

Variational Shapley Network: A Probabilistic Approach to Self-Explaining Shapley values with Uncertainty Quantification

Mert Ketenci¹ Iñigo Urteaga² Victor Alfonso Rodriguez³ Noémie Elhadad^{1,3} Adler Perotte³

Abstract

Shapley values have emerged as a foundational tool in machine learning (ML) for elucidating model decision-making processes. Despite their widespread adoption and unique ability to satisfy essential explainability axioms, computational challenges persist in their estimation when (i) evaluating a model over all possible subset of input feature combinations, (ii) estimating model marginals, and (iii) addressing variability in explanations. We introduce a novel, self-explaining method that simplifies the computation of Shapley values significantly, requiring only a single forward pass. Recognizing the deterministic treatment of Shapley values as a limitation, we explore incorporating a probabilistic framework to capture the inherent uncertainty in explanations. Unlike alternatives, our technique does not rely directly on the observed data space to estimate marginals; instead, it uses adaptable baseline values derived from a latent, feature-specific embedding space, generated by a novel masked neural network architecture. Evaluations on simulated and real datasets underscore our technique’s robust predictive and explanatory performance.

1. Introduction and Related Work

Shapley values (Shapley et al., 1953) — rooted in cooperative game theory and the field of transferable utility — have gained significant attention in the ML community, emerging as a prominent technique for explaining model decision making (Lundberg & Lee, 2017; Lundberg et al., 2020; Covert & Lee, 2021).

For a supervised model $f : \mathcal{X} \rightarrow \mathcal{Y}$, the Shapley value of feature j with respect to a reference set $\mathcal{C} \subseteq \mathcal{A} = \{1, 2, \dots, d = \dim(\mathbf{x})\}$ is the expected marginal contribu-

tion of feature j across all coalitions, where a coalition s is defined as any subset of features in \mathcal{C} (the typical case sets \mathcal{C} to all indices \mathcal{A}) excluding j . We use \mathbf{x}_s to denote the subset of feature values corresponding to the coalition s ; for $s = \mathcal{A}$, we simply write \mathbf{x} . For instance, for $d = \dim(\mathbf{x}) = 25$ and coalition $s = \{1, 21, 6\}$, \mathbf{x}_s denotes $[x_1, x_{21}, x_6]$. The Shapley value of feature j is mathematically defined as:

$$SV_j := \sum_{s \subseteq \mathcal{C} \setminus j} p(s | \mathcal{C}) (v(s \cup j) - v(s)). \quad (1)$$

The function $v(s)$ denotes the value of each coalition, mathematically defined in Eqn. (2). The probability $p(s | \mathcal{C}) = \frac{|s|!(|\mathcal{C}| - |s| - 1)!}{|\mathcal{C}|!}$ quantifies the likelihood of forming a coalition s . The Shapley value considers the j th element’s contribution to a coalition, by considering the difference in the outcome in its absence. Mathematically, the value function $v(s)$ is defined as

$$v(s) = \int f(\mathbf{x}) p(\mathbf{x}_{\mathcal{A} \setminus s} | \mathbf{x}_s) d\mathbf{x}_{\mathcal{A} \setminus s} - \int f(\mathbf{x}) p(\mathbf{x}) d\mathbf{x}. \quad (2)$$

Typically, when explaining ML models, $f(\mathbf{x})$ is defined as the model output. Consequently, $v(s)$ encapsulates the disparity in the model’s outputs computed by marginalizing over the set $\mathcal{A} \setminus s$ in contrast to the entire set \mathcal{A} .

Shapley values are the unique attribution method to satisfy four key explainability axioms: Efficiency, Null Player (Dummy), Symmetry, and Linearity; underpinning their appeal in model explanation (Merrick & Taly, 2020). We refer to (Rozemberczki et al., 2022) for details on their theoretical foundation. Despite its desirable properties and widespread application, estimating Shapley values remains challenging, mainly when (i) summing over all possible coalitions, i.e., Eqn. (1) (Van den Broeck et al., 2022); (ii) estimating model marginals (Covert et al., 2021), i.e., Eqn. (2); and (iii) generating reliable explanations when there is considerable variability in how features affect the response, i.e., accounting for potential randomness in $f(\mathbf{x})$.

Recent research on the first challenge involves solving a post-hoc weighted-least squares problem (Lundberg & Lee, 2017; Covert et al., 2020; Adebayo et al., 2021). While these techniques provide insight into black-box models,

¹Department of Computer Science, Columbia University, New York, USA ²Basque Center for Applied Mathematics, Basque Foundation for Science, Basque, Spain ³Department of Biomedical Informatics, Columbia University, New York, USA. Correspondence to: Mert Ketenci <mk4139@columbia.edu>.

they come with certain drawbacks. Specifically, they may be overly sensitive to slight input changes (Ghorbani et al., 2019), may not always align with the original black-box model’s decisions (Rudin, 2019), and might require extensive sampling for precise explanations (Jethani et al., 2021). FastSHAP proposed an approach to learn Shapley values in a single forward pass (Jethani et al., 2021). However, it requires training multiple neural networks sequentially, which is computationally demanding. *In this work, we propose a self-explaining procedure that requires training a single network.*

The second main challenge with Shapley value computation is on model marginal estimation, as required by the definition in Eqn. (1). In practice, $p(\mathbf{x}_{A \setminus s} | \mathbf{x}_s)$ is analytically unavailable and often, the empirical data distribution is employed. However, this approach is problematic whenever input features are continuous; hence, the empirical distribution sparse. Common solutions estimate model marginals using various approximate distributions, ranging from the product of input marginals to the joint or uniform distribution over inputs (Datta et al., 2016; Lundberg & Lee, 2017; Strumbelj & Kononenko, 2010). However, these can be misleading when input features are correlated. We refer the reader to Covert et al. (2021) for a detailed overview on marginalization techniques and their challenges.

More recently, Sundararajan & Najmi (2020) proposed to use baseline values to replace marginalized variables for Shapley value computation. Covert et al. (2021) showed that training a model by replacing features with baseline values, independently, allows for learning models marginalized by the input conditional distribution. Jethani et al. (2021) used baseline values that are outside of the observed input space to make distinguishing marginals easier. Yet, Covert et al. (2021) emphasized the challenges inherent to baselines in continuous domains, due to the potential misrepresentations induced by them, skewing Shapley values because of the estimated poor marginals. *We address this challenge by defining feature embeddings and baseline values within a latent, learned embedding space. We demonstrate that this approach leads to better performance compared to former alternatives.*

The third challenge relates to the fact that the Shapley values are commonly treated as deterministic entities. This perspective largely stems from the practice of non-probabilistic ML models delivering singular deterministic outputs. Our research demonstrates that this simplification may overlook critical insights, emphasizing the importance of acknowledging the uncertainty inherent in explanations (Chan et al., 2020; Alaa & Van Der Schaar, 2020; Lee et al., 2020). While some post-hoc techniques quantify the uncertainty of their Shapley value estimates, they mainly address uncertainty from Monte Carlo approximations (Covert & Lee, 2021;

Slack et al., 2021). Therefore, they miss the inherent uncertainty in model outputs, vital for robust explanations and understanding why explanations may differ for similar data.

Reasoning about explanation uncertainty is important in real-world applications. Take, for example, the task of deducing Shapley values from an ML model trained to detect dolphins in images. This model is likely to associate blue pixels with dolphins, since they relate to water. Yet, blue pixels are also indicative of the sky, leading to high predictive variance. The question then arises: Can we rely on the Shapley values of such uncertain features? This issue echoes the observations of Alvarez-Melis & Jaakkola (2018). Our work explores the reasons behind this phenomenon, and proposes a framework to address it. Namely, we ask: What if $f(\mathbf{x})$ in Eqn. (2) is a random function (e.g., a Gaussian process)? Should we then also treat SV_j as random? We answer this question positively. We provide an illustrative example in Appx. 5.1 of how, in the presence of randomness, computing Shapley values based on a deterministic ML model is insufficient. Hence, *we utilize a probabilistic framework to account for the uncertainty in data generating processes (DGPs), quantifying how much to trust a given feature’s Shapley value.*

Our contributions are as follows:

1. **We model Shapley values as random variables:** We define stochastic Shapley values (SSVs) $\varphi_j \sim p(\varphi_j | \mathbf{x})$, and write ϕ_j for the expectation over their conditional probability: $\phi_j = \mathbb{E}_{p(\varphi_j | \mathbf{x})} \{\varphi_j\}$.¹ In what follows, we refer to ϕ_j as defined here as the expected Shapley value (ESV).
2. **Self-explaining, probabilistic SSV inference:** We posit per-feature, conditional Gaussian prior densities over SSVs φ_j and, to learn the generative parameters of the SSV prior, devise a variational objective for their regularized inference — guiding prior SSV parameters for it to distribute around each ESV, ϕ_j . To the best of our knowledge, our work is the first attempt to modeling and learning Shapley values in a probabilistic, self-explaining manner.
3. **Explaining uncertainty in model outputs:** We posit a SSV conditional likelihood that allows for capturing the uncertainty in model outputs across φ_j s, producing uncertainty estimates over SSVs that add up to the total predictive uncertainty. We achieve so by utilizing an additive SSV response likelihood, with an amortized variance of the conditional SSV prior.
4. **Efficient modeling and processing of variable-length inputs:** We introduce a masked neural network architecture for efficient processing and marginalization of variable-length, continuous data. In addition, we use

¹Note that, $\phi_j = SV_j$, when $f(\mathbf{x})$ is deterministic.

baseline values in a learned embedding space rather than in input space \mathcal{X} , for accurate marginalization.

5. Accurate Shapley value estimation and uncertainty quantification: We show in synthetic and real datasets how the proposed method learns SSV distributions centered around the ESVs, with informative uncertainty quantification of the stochastic effects observed in data.

2. Variational Shapley Network (VSN)

2.1. VSN’s Generative Story

Let $\mathcal{D} = \{\mathbf{x}_c^{(i)}, y^{(i)}\}_{i=1}^N$ be a set of partially observed input and response pairs. We assume that $\mathbf{x}^{(i)} = [\mathbf{x}_{\mathcal{C}_i}^{(i)}, \mathbf{x}_{\mathcal{M}_i}^{(i)}]$ where \mathcal{C}_i and \mathcal{M}_i refer to conditioned (observed) and marginalized (missing) indices. Hence, $\mathbf{x}_{\mathcal{C}_i}^{(i)}$ can be of variable length across instances, and $\mathcal{C}_i \cup \mathcal{M}_i = \mathcal{A}$.² We pose a Shapley value-based probabilistic model, where $\Phi^{(i)} = [\varphi_j^{(i)}]_{j \in \mathcal{A}}$ denotes the set of SSVs. For input data instance $\mathbf{x}_c^{(i)}$ and the observed response $y^{(i)}$, VSN assumes the following DGP:

There is a parametric, data-conditional SSV prior per input-feature j , $\mathcal{N}(\mu_{\theta_j}(\mathbf{x}_c), \sigma_{\psi_j}^2(\mathbf{x}_c))$, where $\{\theta_j, \psi_j\}_{j \in \mathcal{A}}$ are learnable parameters of per feature mean and variance data-dependent functions.

For each input data point $\mathbf{x}_c^{(i)}$, $i = \{1, \dots, N\}$:

1. Draw per feature j stochastic Shapley values, each from its conditional SSV prior:

$$\varphi_j^{(i)} | \mathbf{x}_c^{(i)} \sim \mathcal{N}(\mu_{\theta_j}(\mathbf{x}_c^{(i)}), \sigma_{\psi_j}^2(\mathbf{x}_c^{(i)})), \quad \forall j \in \mathcal{A}$$

2. Draw a response from the data emission distribution, conditioned on SSVs:

$$y^{(i)} | \Phi^{(i)} \sim p(y^{(i)} | \Phi^{(i)}).$$

With VSN’s DGP, we accommodate flexible, non-linear functions $\mu_{\theta_j}(\mathbf{x}_c)$ and $\sigma_{\psi_j}^2(\mathbf{x}_c)$ (e.g., neural networks) with variable-length input features. The rationale for defining the SSV prior based on partially observed data \mathbf{x}_c (i.e., with variable length inputs) stems from the necessity to learn the marginals for computing Shapley values, an approach also discussed by Covert et al. (2021) and Jethani et al. (2021).

By inspection of the DGP, we observe the following: (i) $\mu_{\theta_j}(\mathbf{x}_c)$ corresponds the expected value of the SSV, i.e., $\mathbb{E}_{p(\varphi_j | \mathbf{x}_c)} \{\varphi_j\}$; and (ii), $\sigma_{\psi_j}^2(\mathbf{x}_c)$ corresponds to the variance (uncertainty measure) of SSVs.

For certain data-likelihood choices, e.g., for the Gaussian additive linear SSV case with $y^{(i)} | \Phi^{(i)} \sim \mathcal{N}(\phi_0 + \sum_{j \in \mathcal{A}} \varphi_j^{(i)}, \sigma_0^2)$, we can compute the prior pre-

²Moving forward, we omit the subscript i in \mathcal{C}_i , and use \mathcal{C} , although we note that they are distinct for each individual example.

dictive distribution analytically (see Appx. 5.2):

$$y^{(i)} | \mathbf{x}_c^{(i)} \sim \mathcal{N}(\mu_{\text{tot}}(\mathbf{x}_c^{(i)}), \sigma_{\text{tot}}^2(\mathbf{x}_c^{(i)})), \quad (3)$$

where we define the total prior predictive mean $\mu_{\text{tot}}(\mathbf{x}_c^{(i)}) = \phi_0 + \sum_{j \in \mathcal{A}} \mu_{\theta_j}(\mathbf{x}_c^{(i)})$, and the total prior predictive variance $\sigma_{\text{tot}}^2(\mathbf{x}_c^{(i)}) = \sigma_0^2 + \sum_{j \in \mathcal{A}} \sigma_{\psi_j}^2(\mathbf{x}_c^{(i)})$. ESVs quantify the deviation of a specific prediction from the average predictions across the dataset. Hence, incorporation of the ϕ_0 term in the DGP likelihood is essential to embody this average.

2.2. Inference and Learning

We argue here why a variational inference-based approach is needed to learn the SSVs of interest, i.e., to learn generative model’s priors that are centered around the ESV of each feature: $\mu_{\theta_j}(\mathbf{x}_c^{(i)}) \rightarrow \text{ESV}_j^{(i)} = \phi_j^{(i)}$. We begin by discussing why maximum likelihood inference does not suffice.

Maximum likelihood. The joint data likelihood of the DGP over random variables \mathbf{y} and Φ , given \mathbf{X}_c , is:

$$\ell = p(\mathbf{y}, \Phi | \mathbf{X}_c) = \prod_{i=1}^N \underbrace{p(y^{(i)} | \Phi^{(i)})}_{\ell^{(i)}} \prod_{j \in \mathcal{A}} p(\varphi_j^{(i)} | \mathbf{x}_c^{(i)}). \quad (4)$$

When possible, we integrate out the latent SSV random variables to attain the marginal log-likelihood

$$\mathcal{L} = \sum_{i=1}^N \log \int \ell^{(i)} d\Phi^{(i)}, \quad (5)$$

which is analytically tractable, e.g., for the Gaussian additive linear SSV case:

$$\sum_{i=1}^N \log \mathcal{N}(\mu_{\text{tot}}(\mathbf{x}_c^{(i)}), \sigma_{\text{tot}}^2(\mathbf{x}_c^{(i)})). \quad (6)$$

While direct maximization of Eqn. (5) enables data-driven estimation of all model parameters $\Theta = \{\phi_0, \{\theta_j, \psi_j\}_{j \in \mathcal{A}}\}$, nothing enforces $\varphi_j^{(i)}$ ’s to distribute around ESVs $\phi_j^{(i)}$. *In other words, there is no incentive within \mathcal{L} to find Θ that enforces $\varphi_j^{(i)}$ to distribute around the ESVs of interest.*

We overcome this limitation with variational inference (Blei et al., 2016), where we restrict the search space of learnable parameters Θ via variational regularization, an efficient strategy that helps with self-explainability (Alvarez Melis & Jaakkola, 2018).

Variational inference. Variational methods lower-bound the marginal log-likelihood \mathcal{L} for any variational family $q \in \mathcal{Q}$; or equivalently, minimize the distance between the assumed variational distribution q and the true target p . In our case, a variational *solution* $q_{\text{sol}}(\Phi^{(i)} | \mathbf{x}_c^{(i)}) = \prod_{j \in \mathcal{A}} q_{\text{sol}}(\varphi_j^{(i)} | \mathbf{x}_c^{(i)})$ and the true model posterior $p(\Phi^{(i)} | \mathbf{x}_c^{(i)}, y^{(i)})$, where we enforce the variational family to center around the DGP’s per-feature ESVs, $\phi_j^{(i)}$. In order to accomplish this, we (i) enforce the inferred variational solution to be aligned with the ESVs of the DGP,

and (ii) pull the posit prior close to this inferred ESVs, for which we turn into the variational machinery.

We choose a Gaussian variational family $q_{\text{sol}}(\varphi_j^{(i)} | \mathbf{x}_c^{(i)}) = \mathcal{N}\left(\mu_{\text{sol}_j}(\mathbf{x}_c^{(i)}), \sigma_{\psi_j}^2(\mathbf{x}_c^{(i)})\right)$, where we enforce the expected value of the variational solution to obey

$$\mu_{\text{sol}_j}(\mathbf{x}_c^{(i)}) = \sum_{s \subseteq \mathcal{C} \setminus \{j\}} p(s | \mathcal{C}) (v_{\text{sol}}(s \cup \{j\}) - v_{\text{sol}}(s)),$$

with $v_{\text{sol}}(s) := \mu_{\text{tot}}(\mathbf{x}_s^{(i)})$. (7)

We constrain the variational solution’s per-feature j expected values to be distributed around each per-feature ESV of the assumed DGP, with uncertainty determined by the prior’s variance $\sigma_{\psi_j}^2(\mathbf{x}_c^{(i)})$. Namely, the j -th mean of the variational solution $\mu_{\text{sol}_j}(\mathbf{x}_c^{(i)})$ is equal to the DGP’s j -th ESV. Based on the theory of Covert et al. (2021) and the training procedure we describe in Alg. 1, v_{sol} represents the value function that describes the DGP’s expected model outputs marginalized by data conditionals, and $\mu_{\text{sol}_j}(\mathbf{x}_c^{(i)})$ — which can be computed in a single forward pass — converges to $ESV_j^{(i)}$ (Appx. 5.3).

We strategically align the variational distribution’s variance with the DGP prior, amortizing these shared learnable parameters $\sigma_{\psi_j}^2(\mathbf{x}_c^{(i)})$. This choice leads to smaller divergence, and tightens the lower-bound. To enforce each $\sigma_{\psi_j}^2(\mathbf{x}_c^{(i)})$ to model its corresponding j th SSV uncertainty, we limit its input as described in Sec. 2.5.

Since q_{sol} is defined in terms of the SSV prior’s sufficient statistics — the solution’s expected value depends on the prior’s predictive mean, and the solution’s variance is equal to the prior’s variance — our use of variational inference can be understood as a regularization of the posit prior. Namely, we regularize the DGP model family, which is tied to the data-conditional SSV prior, to ensure that learned (latent) SSV variables center around the DGP’s ESVs.

Evidence lower-bound. Using the proposed variational family, we derive the variational inference objective, with full details provided in Appx. 5.5:

$$\mathcal{L} \geq \sum_{i=1}^N \mathbb{E}_{q_{\text{sol}}(\Phi^{(i)} | \mathbf{x}^{(i)})} \{\log p(y^{(i)} | \Phi^{(i)})\} - \mathcal{R}, \text{ and}$$

$$\mathcal{R} = \sum_{i=1}^N \sum_{j \in \mathcal{A}} \underbrace{D_{\text{KL}}(q_{\text{sol}}(\varphi_j^{(i)} | \mathbf{x}_c^{(i)}) \| p(\varphi_j^{(i)} | \mathbf{x}_c^{(i)}))}_{\mathcal{R}_{ij}}. \quad (8)$$

Remark 2.1. Although the SSV prior is defined so that it’s expectation matches the ESV, the maximum likelihood solution of the first loss term above — in the absence of variational constraint \mathcal{R} — would not necessarily enforce alignment of the SSV prior means with the ESV values of interest, leaving the DGP as a mere data-generation analogy. Notably, as \mathcal{R} goes to 0, the SSV priors distribute around the

ESVs. Consequently, the expectation across \mathcal{D} of the sum of the means of the SSV priors converges to 0 (a detailed derivation is provided in Appx. 5.4). Therefore, ϕ_0 tends towards the expected model predictions across the empirical data distribution \mathcal{D} . This observation provides useful model convergence diagnostics, e.g., as shown in Fig. 2.

For the assumed generative process and variational families, \mathcal{R}_{ij} in Eqn. (8) obeys the analytical solution:

$$\frac{(\mu_{\text{sol}_j}(\mathbf{x}_c^{(i)}) - \mu_{\theta_j}(\mathbf{x}_c^{(i)}))^2}{2\sigma_{\psi_j}^2(\mathbf{x}_c^{(i)})}. \quad (9)$$

This regularization term may seem similar to the loss in kernel-based Shapley value algorithms (Lundberg & Lee, 2017; Covert & Lee, 2021), and in particular, FastSHAP (Jethani et al., 2021). On the contrary, unlike in previous works, our value and explanatory functions are defined by a shared network, learned jointly via variational inference. More importantly, our KL-divergence term does not impose a weighted-least squares problem, avoiding coalition sampling over an L2 loss. Finally, our regularization incorporates the uncertainty in outputs; hence, ∇_{θ_j} — weighted by $\sigma_{\psi_j}^2$ — will be smaller for high-uncertainty regions.

2.3. A Tighter and Computationally More Efficient Variational Inference for VSN

Implementing Eqn. (8) is computationally challenging, as it requires computing $q_{\text{sol}}(\Phi^{(i)} | \mathbf{x}^{(i)})$ — of complexity $\mathcal{O}(2^{|\mathcal{C}|})$ — to calculate $\mathbb{E}_{q_{\text{sol}}(\Phi^{(i)} | \mathbf{x}^{(i)})} \{\log p(y^{(i)} | \Phi^{(i)})\}$. To circumvent such computational complexity, we formulate the following:

Proposition 2.2. $\mathbb{E}_{q_{\text{sol}}(\Phi^{(i)} | \mathbf{x}^{(i)})} \left\{ f\left(\phi_0 + \sum_{j \in \mathcal{A}} \varphi_j^{(i)}\right) \right\}$ is equal to $\mathbb{E}_{p(\Phi^{(i)} | \mathbf{x}^{(i)})} \left\{ f\left(\phi_0 + \sum_{j \in \mathcal{A}} \varphi_j^{(i)}\right) \right\}$.

Proof. Please see Appx. 5.6 for a detailed proof. \square

Using Proposition 2.2 and Jensen’s inequality, we can rewrite (see Appx. 5.7 for a detailed derivation):

$$\mathcal{L} \geq \mathcal{V} = \mathcal{L} - b\mathcal{R} \geq \sum_{i=1}^N \mathbb{E}_{q_{\text{sol}}(\Phi^{(i)} | \mathbf{x}^{(i)})} \{\log p(y^{(i)} | \Phi^{(i)})\} - \mathcal{R}$$

$$= \sum_{i=1}^N \mathbb{E}_{p(\Phi^{(i)} | \mathbf{x}^{(i)})} \{\log p(y^{(i)} | \Phi^{(i)})\} - \mathcal{R}$$

for $0 \leq b \leq 1$. (10)

Remark 2.3. For $b = 0$, the above lower-bound becomes exact, with $\mathcal{V} = \mathcal{L}$. However, this is not desired due to aforementioned reasons. While maximizing \mathcal{L} encourages finding a model that explains \mathbf{y} and its variance, \mathcal{R} guides, via KL minimization of the variational solution, each SSV prior to distribute around ESVs $\phi_j^{(i)}$.

2.4. VSN Learning via Stochastic Gradient Descent

To maximize the lower-bound \mathcal{V} in Eqn. (10), we must compute gradients of both of its terms. \mathcal{L} and \mathcal{R} already allow for mini-batching over the dataset, and for the cases where \mathcal{L} is analytically tractable, we can readily compute its unbiased gradients efficiently (Bishop & Nasrabadi, 2006).

However, calculating $\mu_{\text{so1}_j}(\mathbf{x}_c^{(i)})$ in \mathcal{R}_{ij} requires a sum that still scales in $\mathcal{O}(2^{|\mathcal{C}|})$. Notably, an unbiased stochastic estimate of $\mu_{\text{so1}_j}(\mathbf{x}_c^{(i)})$ is available (Castro et al., 2009):

$$\hat{\mu}_{\text{so1}_j}(\mathbf{x}_c^{(i)}, \{\hat{s}_k\}_{k=1}^K) \approx \frac{\sum_{k=1}^K \mu_{\text{tot}}(\mathbf{x}_{\hat{s}_k}^{(i)}, x_j^{(i)}) - \mu_{\text{tot}}(\mathbf{x}_{\hat{s}_k}^{(i)})}{K}, \quad (11)$$

where $\hat{s}_k \sim p(s | \mathcal{C})$ for $k = 1, \dots, K$. For the gradients of \mathcal{R} , one may be tempted to use the sample based version of the analytical solution in Eqn. (11), i.e.,

$$\widehat{\mathcal{R}}_{ij}(\mathbf{x}_c^{(i)}, \{\hat{s}_k\}_{k=1}^K) = \frac{\overbrace{(\hat{\mu}_{\text{so1}_j}(\mathbf{x}_c^{(i)}, \{\hat{s}_k\}_{k=1}^K) - \mu_{\theta_j}(\mathbf{x}_c^{(i)}))^2}^{\Delta_{ij}(\{\hat{s}_k\}_{k=1}^K)}}{2\sigma_{\psi_j}^2(\mathbf{x}_c^{(i)})}, \quad (12)$$

which, unfortunately, leads to biased gradients. We instead propose a surrogate, unbiased alternative — in which for notation clarity, and because we use a single coalition sample in practice $\hat{s}_k \sim p(s | \mathcal{C})$, $K = 1$, we omit subscript k .

Proposition 2.4. *The surrogate function*

$$\widehat{\mathcal{R}}_{ij}(\mathbf{x}_c^{(i)}, \hat{s}, \hat{s}) = d \frac{\Delta_{ij(i)}(\hat{s}) \Delta_{ij(i)}(\hat{s})}{2\sigma_{\psi_j(i)}^2(\mathbf{x}_c^{(i)})}, \quad (13)$$

where $j(i) \sim \mathcal{U}(1, d)$, \hat{s} and \hat{s} are sampled independently ($\hat{s} \perp\!\!\!\perp \hat{s}$), and the gradients of $\Delta_{ij(i)}(\hat{s})$ are detached, provides unbiased estimates for $\nabla_{\Theta} \mathcal{R}$.

Proof. Please see Appx. 5.8 for a detailed proof. \square

By combination of our propositions and the objective \mathcal{V} , we introduce a mini-batched variational objective to maximize,³

$$\begin{aligned} & \hat{\mathcal{V}}(\Theta | \{\mathbf{x}_c^{(i)}, y^{(i)}\}_{i=1}^M, \{\hat{s}^{(i)}, \hat{s}^{(i)}\}_{i=1}^M, \{j(i)\}_{i=1}^M, \beta) \\ &= \frac{N}{M} \left(\sum_{i=1}^M \mathcal{L}_i - \beta \frac{\Delta_{ij(i)}(\hat{s}_i^{(i)}) \Delta_{ij(i)}(\hat{s}_i^{(i)})}{\sigma_{\psi_j(i)}^2(\mathbf{x}_c^{(i)})} \right), \end{aligned} \quad (14)$$

which enables the design of a mini-batch-based stochastic gradient descent (SGD) learning algorithm for VSN, described in Algorithm 1.

2.5. Network Architecture

In this section, we describe how we leverage neural networks to model SSV prior parameters, $\mu_{\theta_j}(\mathbf{x}_c^{(i)})$ and $\sigma_{\psi_j}^2(\mathbf{x}_c^{(i)})$, the rationale of our framework, and the proposed masked neural network architecture that enables their efficient computation across features.

³We shortly denote $\frac{bd}{2} = \beta$, and note that each $\{\hat{s}_i^{(i)}, \hat{s}_i^{(i)}\}$ pair are sampled independently for each $\mathbf{x}_c^{(i)}$.

Algorithm 1 Mini-batch SGD learning of VSN.

Input: Dataset \mathcal{D} , and hyperparameters β, p, M
 $\Theta \leftarrow$ Initialize parameters
while not converged **do**
 Draw $\mathcal{C}_i = \{j | \mathbb{1}_j = 1, \forall j \in \mathcal{A}\} | \mathbb{1}_j \sim \text{Ber}(p), \forall i$
 Draw $\{\mathbf{x}_c^{(i)}, y^{(i)}\}_{i=1}^M \sim \mathcal{D}$
 Draw $\{\hat{s}^{(i)}, \hat{s}^{(i)}\}_{i=1}^M \sim p(s | \mathcal{C})$ for each $\{\mathbf{x}_c^{(i)}, y^{(i)}\}$
 Draw $\{j(i)\}_{i=1}^M \sim \mathcal{U}(1, d)$ for each $\{\mathbf{x}_c^{(i)}, y^{(i)}\}$
 $g \leftarrow \nabla_{\Theta} \hat{\mathcal{V}}(\Theta | \{\mathbf{x}_c^{(i)}, y^{(i)}\}_{i=1}^M, \{\hat{s}^{(i)}, \hat{s}^{(i)}\}_{i=1}^M, \{j(i)\}_{i=1}^M, \beta)$
 $\Theta \leftarrow$ Update using gradients g
end while
Output: Explainable VSN model, with parameters Θ

Overall architecture. We begin by mapping the inputs $\mathbf{x} \in \mathcal{X}$ to $Z \in \mathbb{R}^{d \times d_Z}$, where each row of Z represents $\mathbf{z}_j = \text{emb}(x_j)$, calculated in parallel via our masked network architecture (see details below). When marginalizing over x_j , we replace the embedding \mathbf{z}_j of x_j with learnable baseline vector \mathbf{b}_j . Then, we take a linear combination of these embeddings with an affine transformation matrix W , and feed the result into a feedforward network to obtain μ_{θ_j} .

For modeling σ_{ψ_j} , we only consider the detached \mathbf{z}_j and the detached output from μ_{θ_j} . By detaching the gradients, we prevent information flow to the embedding from the variance parameter, which we empirically found beneficial. The choice of restricting the input to the σ_{ψ_j} network, to detached features \mathbf{z}_j and μ_{θ_j} , is to prevent information leakage from other features. This step is taken due to (contrary to μ_{so1}) the lack of variance regularization present in term R_{ij} of Eqn. (9). Specifically, because \mathcal{L} is additive in the uncertainty variables, a model with all features to σ_{ψ_j} as inputs would not have a principle way to allocate the uncertainty across each SSVs' variance parameters. One way to prevent such an information leakage is to only use x_j to model the corresponding SSV uncertainty. However, note that x_j can have multiple SSV mean parameters (i.e., ESVs) depending on other features that participate in coalitions. Therefore, we use information from x_j and its predicted ESV as input to σ_{ψ_j} . We found that our architecture allows for reliable variance allocation, as shown in Fig. 4. We illustrate details of the proposed architecture in Fig. 1.

Rationale for embedded baselines. State-of-the-art techniques use data-space baseline values to model marginals. For example, Yoon et al. (2018) uses a baseline of 0 on inputs to enforce model marginalization. However, using a fixed value in the input space can be misleading, especially for structured data. An alternative is to append a masking vector ξ ⁴ along with the features, that are replaced by base-

⁴In our case, ξ is a matrix repeated (the number of embedding size times) along the second axis, since we replace an entire embedding with a learnable baseline vector.

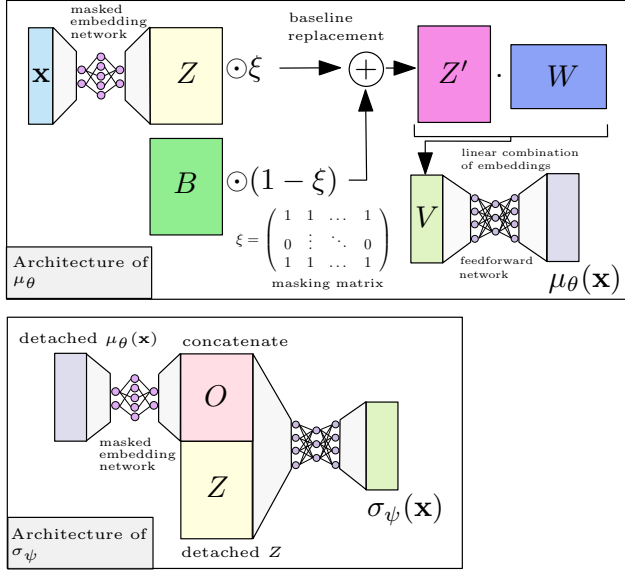


Figure 1. Our novel, masked network architecture. We independently generate latent embedding vectors for each feature, and replace absent features with a baseline vector in this embedding space. We compute a linear combination of these embeddings to arrive at a single vector, which we use as model outputs. To compute the variance, we utilize the information in model predictions and feature representations only, and let the model learn the best variance parameters that utilize these two information sources.

line values (Jethani et al., 2021), which has been shown to be beneficial (Miscouridou et al., 2018).

We, rather than using baseline values in \mathcal{X} , map each x_j to a high-dimensional embedding space, defined as $\mathbf{z}_j = \text{emb}(x_j)$; and when x_j is marginalized, replace \mathbf{z}_j with a learnable baseline embedding \mathbf{b}_j . We empirically demonstrate the superior performance of these approach with results in Table 2 and marginals in Fig. 3.

To embed structured features before inputting them to a network, we apply a distinct neural network-based embedding to each input feature, independently; contrary to previous work advocating for piece-wise linear functions (Gorishniy et al., 2022). Iterating over each $j \in \mathcal{A}$ to produce feature embeddings is computationally expensive, so we propose a masking technique to exploit the inherent parallelism of neural networks.

Masked neural architectures have been widely adopted for various applications, such as natural language processing and density estimation (Vaswani et al., 2017; Devlin et al., 2018; Papamakarios et al., 2017). Our objective and methodology diverge here, as our focus is not on sequential or auto-regressive input-output modeling, but on constructing high-dimensional embeddings contingent upon a singular feature. The masked neural network framework we propose ensures an optimal information propagation across the network’s neurons, enabling the simultaneous generation of continuous embeddings per-feature, in parallel. We provide

a detailed description of the masking-based network below, and an illustrative example in Appx. 5.9.

Masking-based neural network. An L -layer neural network can be represented by $\mathbf{z}_k = \text{act}_k(\mathbf{z}_{k-1} W_k)$, where $\mathbf{z}_0 = \mathbf{x}^\top$ and $z_L = \hat{y}$. We define each $W_k = W'_k \odot M_k$, where M_k are binary $d_1^k \times d_2^k$ masking matrices with $d_2^k \geq d$.

The permeability of the network is determined by the non-zero elements of $M_{1:L} = \prod_{k=1}^L M_k$. In particular, if $M_{1:L}(i, j) > 0$, then there is an information flow from i^{th} feature to j^{th} output neuron (Germain et al., 2015).

We begin by defining our initial masking matrix M_1 as

$$M_1(ij) = \begin{cases} 1, & \text{if } 1 + (i-1)e_1 \leq j \leq ie_1 \mathbb{1}_{i \neq d} + d_2^1 \mathbb{1}_{i=d} \\ 0, & \text{otherwise;} \end{cases}$$

and M_k , for $k > 1$, as $\text{col}_j(M_k) = \text{sgn}(\text{row}_i(M_{1:k-1})^\top)$, for $1 + (i-1)e_k \leq j \leq ie_k \mathbb{1}_{i \neq d} + d_2^k \mathbb{1}_{i=d}$, where $\text{sgn}(\cdot)$ is the sign function, $e_k = \text{nint}(d_2^k/d)$ for $i \in \mathcal{A}$, $k \in \{1, 2, \dots, L\}$, and d_2^L is an integer multiple of d . Here, $\text{nint}(\cdot)$ refers to the nearest integer function. The multiplication of a sequence of such matrices have the following recursion:

$$\text{col}_j(M_{1:k}) = \alpha_i \text{col}_{1+(i-1)e_{k-1}}(M_{1:k-1}), \quad (15)$$

where $1 + (i-1)e_k \leq j \leq ie_k \mathbb{1}_{i \neq d} + d_2^k \mathbb{1}_{i=d}$, and $\alpha_i \in \mathbb{N}^+$ for $i \in \{1, 2, \dots, d\}$. Since d_2^L is an integer multiple of d , the columns of $M_{1:L}$ repeat $\text{col}_{1+(i-1)e_{L-1}}(M_{1:L-1})$ e_L number of times.

Then, $d \times de_L$ matrix $M_{1:L}$ obeys:

$$M_{1:L}(ij) = \begin{cases} \gamma_i, & \text{for } \gamma_i > 0, \text{ if } 1 + (i-1)e_L \leq j \leq ie_L \\ 0, & \text{otherwise.} \end{cases}$$

For instance, for $d = 3$, $d_2^L = 6$ (i.e., $d_Z = e_L = 2$), $M_{1:L}$ is (see a step-by-step example in Appx. 5.9):

$$\prod_{k=1}^L M_k = \begin{bmatrix} \gamma_1 & \gamma_1 & 0 & 0 & 0 & 0 \\ 0 & 0 & \gamma_2 & \gamma_2 & 0 & 0 \\ 0 & 0 & 0 & 0 & \gamma_3 & \gamma_3 \end{bmatrix}.$$

3. Results

In Sec. 3.1, we demonstrate a useful diagnostic to monitor VSN’s learning of ESVs. In Sec. 3.2, we compare our novel masked network architecture’s capability to learn marginals to standard baseline-based feedforward approaches. In Sec. 3.3, we compare VSN’s predictive performance to various benchmark models on several real-world and simulated datasets. In Sec. 3.4, we demonstrate that VSN provides meaningful uncertainty estimates for explanations. Finally, we asses VSN’s explainability on a real-world ICU mortality prediction dataset, where medically trained collaborators interpreted VSN’s output, in Appx. 5.14.

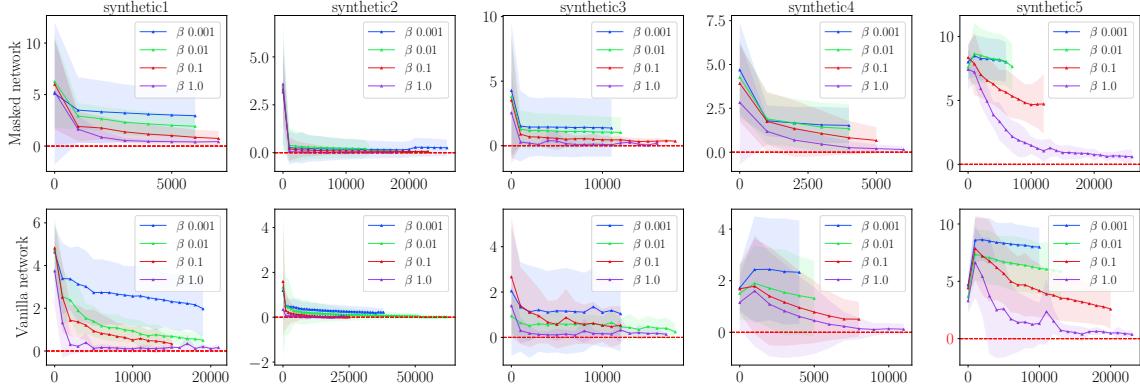


Figure 2. The average of the ESVs over the empirical dataset, $\mathbb{E}_{\mathcal{D}} \{\mu_{\text{tot}}(\mathbf{x}^{(i)}) - \phi_0\}$, over training epochs. Shaded regions are the error values from different cross-validation folds. It is clear that the estimates converge to zero as the model learns — this is most prominent for $\beta = 1$. The VSN objective enables learning ESVs for both masked and simple feedforward network architectures.

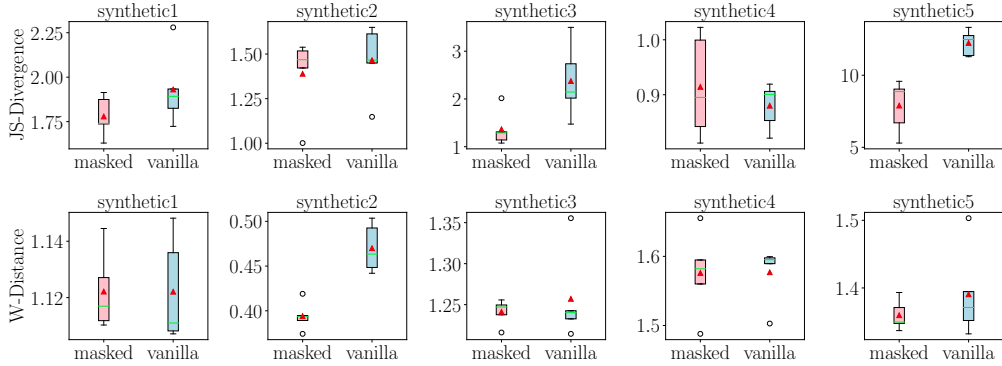


Figure 3. Distance measures of VSN’s marginals to empirical data: comparison of the proposed method and a feedforward NN with baseline replacements. \blacktriangle is the mean and $-$ is the median of results across folds, error bars denote the 1.5 interquartile range.

3.1. VSN’s ESV Learning Diagnostics

We determine if VSN is effectively learning ESVs by examining the evolution of $\mathbb{E}_{\mathcal{D}} \{\mu_{\text{tot}}(\mathbf{x}^{(i)} s) - \phi_0\}$ over training epochs. As highlighted in Sec. 2.2 and proved in Appx. 5.4, the average of the ESVs over the empirical data should converge to 0. Results depicted in Fig. 2 demonstrate that, during VSN training, $\mathbb{E}_{\mathcal{D}} \{\mu_{\text{tot}}(\mathbf{x}^{(i)} s) - \phi_0\} \rightarrow 0$ across different network designs and for different β values. These experiments support VSN’s efficacy and accuracy, with the trend being especially pronounced when $\beta = 1$, i.e., when the variational regularization is most prominent.

3.2. Marginal Distribution Quality over Different Architectures

We assess the quality of model marginals learned by our novel (masked) network architecture compared to a (vanilla) feedforward network that accepts input masking indicators and features replaced by baseline values. To measure the quality of computed marginals, we consider (i) Jensen-Shannon (JS-), and (ii) Wasserstein (W-) distances. Both determine how closely the model’s marginals align with the empirical data marginals, where smaller values are better. We generate samples from both architectures, and measure the distance to ground truth empirical marginals. We weight

the distance measures from each marginal by the frequency that they appear in Eqn. (1), and sum them to present a single comparison metric (see Appx. 5.10 for details). In Fig. 3, we report the interquartile ranges of these metrics over five data splits, and observe that the distance of the masked network’s marginals (both in its mean and median statistics) is closer to the empirical marginals for both metrics. The difference is most apparent for synthetic 1,2,3&5.

3.3. Performance Comparisons to Other ML Models

We here assess the predictive performance of VSN by comparing it to six baselines, across 11 real-world datasets: 7 regression and 4 classification tasks used in the literature. We provide a comprehensive description of baseline models, datasets and the experimental setup in Appx. 5.11. Averaged test-set results are presented in Table 1, with standard error details provided in Appx. 5.12.

From Table 1, we conclude that VSN is a robust competitor to well-known black-box ML models, both for regression and classification tasks. Notably, VSN surpasses other self-explanatory counterparts (highlighted within the dark grey area), with a clear advantage over EBM. We contend this superiority to VSN’s capacity to accommodate all potential

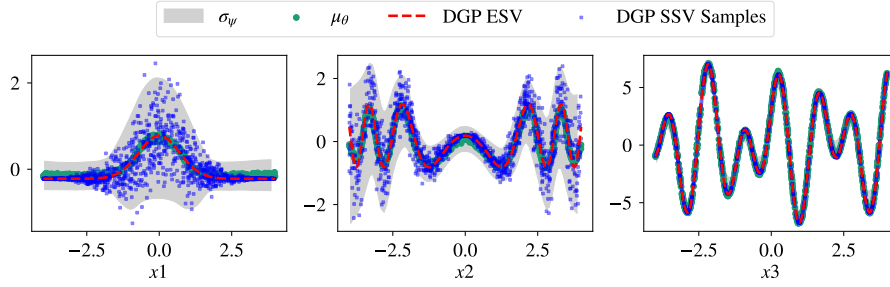


Figure 4. The true DGP’s ESV values (red line), true SSV values as computed in Appx. 5.13 (blue scatter), and the ESV learned by VSN (green scatter) with their corresponding uncertainty intervals (shaded region, 2.5 standard deviations). VSN’s variational solution not only captures the average contribution of each x_j (the expected Shapley values of the DGP) accurately, but also provides credible intervals informing about the full range of the potential attribution of x_j on the DGP’s outputs.

feature interactions at once, contrary to EBM’s necessity of incorporating a different flexible function approximator for each potential feature interaction.

Data	Self-explaining			Black-box			
	VSN	LIN	EBM	RF	LGBM	XGB	DNN
PKSN	0.031	0.867	0.195	0.040	0.072	0.063	0.111
MED	0.447	0.608	0.447	0.448	0.447	0.454	0.467
BIKE	0.010	0.518	0.038	0.008	0.017	0.013	0.019
PUMA	0.285	1.005	0.326	0.303	0.334	0.345	0.225
GAS	0.273	60.93	0.153	0.151	0.152	0.150	0.256
WINE	0.474	0.561	0.508	0.478	0.439	0.433	0.444
ELEV	0.350	0.593	0.385	0.457	0.373	0.373	0.341
FICO	0.774	0.766	0.771	0.770	0.773	0.773	0.771
SPAM	0.977	0.946	0.977	0.983	0.982	0.981	0.967
ICU	0.869	0.851	0.872	0.869	0.874	0.874	0.860
CENS	0.795	0.768	0.825	0.800	0.830	0.831	0.788

Table 1. Averaged results on 11 real-world datasets – see Appx. 5.12 for standard errors. We report RMSE for regression (purple) and PR-AUC for classification (pink) datasets. Lower RMSE and higher PR-AUC scores are better. We indicate best performing models in **bold**, best performing explainable models in **blue**.

Net	β	synth1	synth2	synth3	synth4	synth5
Masked	0.001	0.647	0.003	0.104	0.675	0.430
	0.01	0.637	0.004	0.097	0.674	0.421
	0.1	0.637	0.003	0.114	0.668	0.414
	1	0.595	0.006	0.265	0.665	0.389
Vanilla	0.001	0.718	0.004	0.462	0.679	0.448
	0.01	0.666	0.004	0.358	0.678	0.444
	0.1	0.650	0.007	0.231	0.670	0.439
	1	0.640	0.018	0.782	0.670	0.523

Table 2. RMSE results of VSN over different model architectures and β values. The best results are shown in **bold**. We observe that the masked network outperforms the widely used baseline methods on all datasets (see Appx. 5.11.2 for DGPs).

We additionally scrutinize VSN’s performance across various β values and architectures using five simulated datasets. Results in Table 2 showcase that the proposed masked network design excels in comparison to the conventional approach of handling feature absence — specifically, substituting marginalized values with baseline variables inputted to a standard feedforward network, accompanied by their masking indicators.

Notice in Table 2 how a rise in β correlates with enhanced performance for the masked network strategy. We posit that by establishing a high-dimensional embedding for every feature, the model’s capacity is amplified, which, when aptly regularized, translates to better outcomes.

3.4. VSN Explainability and Uncertainty Quantification

We illustrate the importance of modeling SSVs via a simulated regression dataset, with outputs y defined by additive functional forms that allow for their analytical ESV derivations, according to the ground truth DGP (see Appx. 5.13). The corresponding SSVs and ESVs are illustrated in Fig. 4, along with VSN’s estimated solution, where we note the stochastic nature of the Shapley values of x_1 and x_2 , in comparison to x_3 . We recall that ESVs do not measure the contribution of an individual feature x_j on the stochastic outcome y , but capture how x_j contributes to y , on average — as calculated over conditionals $p(\varphi_j | \mathbf{x})$. Hence, the effect of an individual feature x_j on the outcome can have high variance, as exemplified by the DGP depicted in Fig. 4: there are high uncertainty regions for $-2.5 \leq x_1 \leq 2.5$, $-2.5 \geq x_2$ and $x_2 \geq 2.5$. On the contrary, the low uncertainty region for x_3 implies that the effect of x_3 on y is exactly the ESV for any data point: i.e., $p(\varphi_3 | \mathbf{x}) \sim \delta(\varphi_3 - f(x_3))$.

Fig. 4 showcases that VSN successfully identifies the SSV that has no uncertainty (x_3), while outputting high uncertainty regions — mid-range of x_1 values, and extreme values of x_2 — for the cases where the true effect of the features (x_1 and x_2) on the output y varies widely around the ESV. Knowledge of this uncertainty is critical for trusting the provided explanations: while conclusions drawn by VSN on the output attribution of feature x_3 is certain and trustworthy, there is uncertainty on how each observed x_1 and x_2 feature value may impact y . We emphasize that VSN correctly identifies the deterministic dependencies of the DGP (x_3) and, at the same time, quantifies the uncertainty around the stochastic effects (x_1 and x_2).

4. Conclusion

We introduced Variational Shapley Network (VSN), a self-explanatory probabilistic model with a variational inference

procedure to estimate distributions over Shapley values. The model accommodates neural network-based learning on a latent embedding space to improve marginal computations, for which we developed an innovative, efficient masked network architecture. VSN provides a diagnostic metric to monitor the learning evolution of ESVs through training. Our experiments indicate that VSN improves marginal distribution computation, hence enhancing overall predictive performance, when compared to various benchmarks across a range of real-world datasets. Importantly, we showcase that VSN’s solution distribution accurately centers around true Shapley values, and provides useful uncertainty quantification of the stochastic effects inherent in observed data.

5. Broader impact and ethical aspects.

Our work presents advancements to the field of explainable machine learning. There are many potential societal consequences of our work, specially those related to the use of ML for elucidating model decision-making processes in real-life applications. However, the impact is broad enough to highlight any specific one here.

References

- Adebayo, J., Muelly, M., Abelson, H., and Kim, B. Post hoc explanations may be ineffective for detecting unknown spurious correlation. In *International conference on learning representations*, 2021.
- Alaa, A. and Van Der Schaar, M. Discriminative jackknife: Quantifying uncertainty in deep learning via higher-order influence functions. In *International Conference on Machine Learning*, pp. 165–174. PMLR, 2020.
- Alvarez Melis, D. and Jaakkola, T. Towards robust interpretability with self-explaining neural networks. *Advances in neural information processing systems*, 31, 2018.
- Alvarez-Melis, D. and Jaakkola, T. S. On the robustness of interpretability methods. *arXiv preprint arXiv:1806.08049*, 2018.
- Bishop, C. M. and Nasrabadi, N. M. *Pattern recognition and machine learning*, volume 4. Springer, 2006.
- Blei, D. M., Kucukelbir, A., and McAuliffe, J. D. Variational Inference: A Review for Statisticians. <https://arxiv.org/abs/1601.00670v9>, January 2016.
- Caruana, R., Lou, Y., Gehrke, J., Koch, P., Sturm, M., and Elhadad, N. Intelligible Models for Healthcare: Predicting Pneumonia Risk and Hospital 30-day Readmission. In *Proceedings of the 21th ACM SIGKDD international conference on knowledge discovery and data mining*, pp. 1721–1730, 2015.
- Castro, J., Gómez, D., and Tejada, J. Polynomial calculation of the shapley value based on sampling. *Computers & Operations Research*, 36(5):1726–1730, 2009.
- Chan, A., Alaa, A., Qian, Z., and Van Der Schaar, M. Unlabelled data improves bayesian uncertainty calibration under covariate shift. In *International conference on machine learning*, pp. 1392–1402. PMLR, 2020.
- Chen, T. and Guestrin, C. Xgboost: A Scalable Tree Boosting System. In *Proceedings of the 22nd ACM SIGKDD International Conference on Knowledge Discovery and Data Mining*, pp. 785–794, 2016.
- Cortez, P., Cerdeira, A., Almeida, F., Matos, T., and Reis, J. Modeling wine preferences by data mining from physicochemical properties. *Decision support systems*, 47(4): 547–553, 2009.
- Covert, I. and Lee, S.-I. Improving kernelshap: Practical shapley value estimation using linear regression. In *International Conference on Artificial Intelligence and Statistics*, pp. 3457–3465. PMLR, 2021.
- Covert, I., Lundberg, S. M., and Lee, S.-I. Understanding global feature contributions with additive importance measures. *Advances in Neural Information Processing Systems*, 33:17212–17223, 2020.
- Covert, I. C., Lundberg, S., and Lee, S.-I. Explaining by removing: A unified framework for model explanation. *The Journal of Machine Learning Research*, 22(1):9477–9566, 2021.
- Datta, A., Sen, S., and Zick, Y. Algorithmic transparency via quantitative input influence: Theory and experiments with learning systems. In *2016 IEEE symposium on security and privacy (SP)*, pp. 598–617. IEEE, 2016.
- Devlin, J., Chang, M.-W., Lee, K., and Toutanova, K. Bert: Pre-training of deep bidirectional transformers for language understanding. *arXiv preprint arXiv:1810.04805*, 2018.
- Fanaee-T, H. Bike Sharing Dataset. UCI Machine Learning Repository, 2013. DOI: <https://doi.org/10.24432/C5W894>.
- FICO. Fico explainable machine learning challenge. <https://community.fico.com/s/explainable-machine-learning-challenge>, 2018.
- Flamary, R., Courty, N., Gramfort, A., Alaya, M. Z., Boisbunon, A., Chambon, S., Chapel, L., Corenflos, A., Fatras, K., Fournier, N., Gautheron, L., Gayraud, N. T., Janati, H., Rakotomamonjy, A., Redko, I., Rolet, A., Schutz, A., Seguy, V., Sutherland, D. J., Tavenard, R., Tong, A., and

- Vayer, T. Pot: Python optimal transport. *Journal of Machine Learning Research*, 22(78):1–8, 2021. URL <http://jmlr.org/papers/v22/20-451.html>.
- Germain, M., Gregor, K., Murray, I., and Larochelle, H. Made: Masked autoencoder for distribution estimation. In *International conference on machine learning*, pp. 881–889. PMLR, 2015.
- Ghahramani, Z. The pumadyn datasets. *J. Complex*, pp. 1–6, 1996.
- Ghorbani, A., Abid, A., and Zou, J. Interpretation of neural networks is fragile. In *Proceedings of the AAAI conference on artificial intelligence*, volume 33, pp. 3681–3688, 2019.
- Goldberger, A. L., Amaral, L. A., Glass, L., Hausdorff, J. M., Ivanov, P. C., Mark, R. G., Mietus, J. E., Moody, G. B., Peng, C.-K., and Stanley, H. E. Physiobank, Physiokit, and Physionet: components of a new research resource for complex physiologic signals. *circulation*, 101(23):e215–e220, 2000.
- Gorishniy, Y., Rubachev, I., and Babenko, A. On embeddings for numerical features in tabular deep learning. *Advances in Neural Information Processing Systems*, 35: 24991–25004, 2022.
- Hopkins, M., Reeber, E., Forman, G., and Suermondt, J. Spambase. UCI Machine Learning Repository, 1999. DOI: <https://doi.org/10.24432/C53G6X>.
- Jethani, N., Sudarshan, M., Covert, I. C., Lee, S.-I., and Ranganath, R. Fastshap: Real-time shapley value estimation. In *International Conference on Learning Representations*, 2021.
- Ke, G., Meng, Q., Finley, T., Wang, T., Chen, W., Ma, W., Ye, Q., and Liu, T.-Y. Lightgbm: A highly efficient gradient boosting decision tree. *Advances in neural information processing systems*, 30, 2017.
- Kohavi, R. Census Income. UCI Machine Learning Repository, 1996. DOI: <https://doi.org/10.24432/C5GP7S>.
- Lantz, B. *Machine Learning with R: Expert techniques for predictive modeling*. Packt publishing ltd, 2019.
- Lee, H.-S., Zhang, Y., Zame, W., Shen, C., Lee, J.-W., and van der Schaar, M. Robust recursive partitioning for heterogeneous treatment effects with uncertainty quantification. *Advances in Neural Information Processing Systems*, 33:2282–2292, 2020.
- Lou, Y., Caruana, R., Gehrke, J., and Hooker, G. Accurate Intelligible Models with Pairwise Interactions. In *Proceedings of the 19th ACM SIGKDD International Conference on Knowledge Discovery and Data Mining*, pp. 623–631, 2013.
- Lucas, D. Greenhouse Gas Observing Network. UCI Machine Learning Repository, 2015. DOI: <https://doi.org/10.24432/C5JK5M>.
- Lundberg, S. M. and Lee, S.-I. A unified approach to interpreting model predictions. *Advances in neural information processing systems*, 30, 2017.
- Lundberg, S. M., Erion, G., Chen, H., DeGrave, A., Prutkin, J. M., Nair, B., Katz, R., Himmelfarb, J., Bansal, N., and Lee, S.-I. From local explanations to global understanding with explainable ai for trees. *Nature machine intelligence*, 2(1):56–67, 2020.
- Meredith, M., Raffa, J., Ghassemi, M., Pollard, T., Kalanidhi, S., Badawi, O., Matthys, K., and Celi, L. A. Wids (Women in Data Science) Datathon 2020: Icu Mortality Prediction. *Journal of Statistics Education*, 2020.
- Merrick, L. and Taly, A. The explanation game: Explaining machine learning models using shapley values. In *Machine Learning and Knowledge Extraction: 4th IFIP TC 5, TC 12, WG 8.4, WG 8.9, WG 12.9 International Cross-Domain Conference, CD-MAKE 2020, Dublin, Ireland, August 25–28, 2020, Proceedings 4*, pp. 17–38. Springer, 2020.
- Miscouridou, X., Perotte, A., Elhadad, N., and Ranganath, R. Deep survival analysis: Nonparametrics and missingness. In *Machine Learning for Healthcare Conference*, pp. 244–256. PMLR, 2018.
- Nori, H., Jenkins, S., Koch, P., and Caruana, R. Interpretml: A Unified Framework for Machine Learning Interpretability. *arXiv preprint arXiv:1909.09223*, 2019.
- Papamakarios, G., Pavlakou, T., and Murray, I. Masked autoregressive flow for density estimation. *Advances in neural information processing systems*, 30, 2017.
- Pedregosa, F., Varoquaux, G., Gramfort, A., Michel, V., Thirion, B., Grisel, O., Blondel, M., Prettenhofer, P., Weiss, R., Dubourg, V., et al. Scikit-learn: Machine learning in Python. *Journal of Machine Learning Research*, 12:2825–2830, 2011.
- Rozemberczki, B., Watson, L., Bayer, P., Yang, H.-T., Kiss, O., Nilsson, S., and Sarkar, R. The shapley value in machine learning. *arXiv preprint arXiv:2202.05594*, 2022.
- Rudin, C. Stop explaining black box machine learning models for high stakes decisions and use interpretable models instead. *Nature machine intelligence*, 1(5):206–215, 2019.

- Shapley, L. S. et al. A value for n-person games. 1953.
- Slack, D., Hilgard, A., Singh, S., and Lakkaraju, H. Reliable post hoc explanations: Modeling uncertainty in explainability. *Advances in neural information processing systems*, 34:9391–9404, 2021.
- Strumbelj, E. and Kononenko, I. An efficient explanation of individual classifications using game theory. *The Journal of Machine Learning Research*, 11:1–18, 2010.
- Sundararajan, M. and Najmi, A. The many shapley values for model explanation. In *International conference on machine learning*, pp. 9269–9278. PMLR, 2020.
- Tsanas, A., Little, M., McSharry, P., and Ramig, L. Accurate telemonitoring of parkinson’s disease progression by non-invasive speech tests. *Nature Precedings*, pp. 1–1, 2009.
- Van den Broeck, G., Lykov, A., Schleich, M., and Suci, D. On the tractability of shap explanations. *Journal of Artificial Intelligence Research*, 74:851–886, 2022.
- Vaswani, A., Shazeer, N., Parmar, N., Uszkoreit, J., Jones, L., Gomez, A. N., Kaiser, Ł., and Polosukhin, I. Attention is all you need. *Advances in neural information processing systems*, 30, 2017.
- Yoon, J., Jordon, J., and van der Schaar, M. Invase: Instance-wise variable selection using neural networks. In *International Conference on Learning Representations*, 2018.

Appendix

5.1. A Mathematical, Motivating Example

In this section, we provide a mathematical example for deriving Shapley values in two complementary ways: (i) using the true DGP, and (ii) assuming a post-hoc supervised ML model, trained on this DGP. We then compare these two explanations, and explain why (i) is desirable.

Data generating process. Mathematically, we formulate an example DGP as follows: $f_1(x_1) \sim \mathcal{N}\left(x_1, \frac{1}{(x_1-10)^2}\right)$, $f_2(x_2) \sim \mathcal{N}\left(2x_2, \frac{1}{x_2^2}\right)$, $x_1 \sim \mathcal{U}(-10, 10)$, $x_2 \sim \mathcal{U}(-10, 10)$, and $y = f(\mathbf{x}) = f_1(x_1) + f_2(x_2)$.

Derivations based on the true DGP. We calculate SV_1 using the true DGP. We begin by writing the equation for SV_1 :

$$SV_1 = \frac{1}{2} \underbrace{(v(\{1, 2\}) - v(\{2\}))}_{(i)} + \frac{1}{2} \underbrace{(v(\{1\}) - v(\{\}))}_{(ii)} \quad (16)$$

The first term:

$$\begin{aligned} & v(\{1, 2\}) - v(\{2\}) \\ &= y - \int y \mathcal{N}\left(x_1, \frac{1}{(x_1-10)^2}\right) \mathcal{U}(-10, 10) df_1 dx_1 \\ &= f_1(x_1) + f_2(x_2) - f_2(x_2) \\ &= f_1(x_1) \end{aligned} \quad (17)$$

The second term:

$$\begin{aligned} & v(\{1\}) - v(\{\}) \\ &= \int y \mathcal{N}\left(2x_2, \frac{1}{x_2^2}\right) \mathcal{U}(-10, 10) df_2 dx_2 \\ &\quad - \int y \mathcal{N}\left(x_1, \frac{1}{(x_1-10)^2}\right) \mathcal{U}(-10, 10) \mathcal{N}\left(2x_2, \frac{1}{x_2^2}\right) \mathcal{U}(-10, 10) df_1 dx_1 df_2 dx_2 \\ &= f_1(x_1) - 0 \\ &= f_1(x_1) \end{aligned} \quad (18)$$

Hence,

$$SV_1 = \frac{1}{2} (f_1(x_1) + f_1(x_1)) = f_1(x_1) \quad (19)$$

Notice that the SV_1 is random. Precisely, $SV_1 = f_1(x_1) \sim \mathcal{N}\left(x_1, \frac{1}{(x_1-10)^2}\right)$.

We refer to this variable as the stochastic Shapley value (SSV), as it defines an entire distribution rather than a single value. We denote SSVs with φ_j . In this case, φ_1 .

With SSVs at our disposal, we can readily compute the expected Shapley value (ESV), denoted with ϕ .

In this case, $\phi_1 = \mathbb{E}_{p(\varphi_1|x_1)} \{\varphi_1\}$, where $p(\varphi_1 | x_1)$ is defined by the SSV derived using the DGP: $\varphi_1 \sim \mathcal{N}\left(x_1, \frac{1}{(x_1-10)^2}\right)$. Hence, $\phi_1 = x_1$.

The ESV only informs about the expected value of the SSV rather than its entire distribution.

Post-hoc explanations based on a deterministic, supervised ML model. Supervised ML models use summary statistics — typically, the model mean — to describe the response (y), often referred to as the model output. For example, a supervised ML model trained using the mean squared error (MSE) loss would approximate the expected data statistics.

Let us assume there exists a supervised model $f' = f'_1 + f'_2 \in \mathcal{F}$, that is sufficiently flexible and trained with MSE loss on sufficiently large data (generated using the above DGP).

We denote deterministic functions with f' . We then have $f'_1(x_1) \sim \delta(f'_1(x_1) - x_1)$, $f'_2(x_2) \sim \delta(f'_2(x_2) - 2x_2)$, where $y' = f'(\mathbf{x}) = f'_1(x_1) + f'_2(x_2)$.

Without loss of generality, we assume that we have access to $x_1 \sim \mathcal{U}(-10, 10)$ and $x_2 \sim \mathcal{U}(-10, 10)$, and calculate SV_1 using the ML model as follows:

$$SV_1 = \frac{1}{2} \underbrace{(v(\{1, 2\}) - v(\{2\}))}_{(i)} + \frac{1}{2} \underbrace{(v(\{1\}) - v(\{\}))}_{(ii)} \quad (20)$$

The first term:

$$\begin{aligned} & v(\{1, 2\}) - v(\{2\}) \\ &= y' - \int y' \delta(f'_1(x_1) - x_1) \mathcal{U}(-10, 10) df'_1 dx_1 \\ &= f'_1(x_1) + f'_2(x_2) - f'_2(x_2) \\ &= f'_1(x_1) \\ &= x_1 \quad \text{since } f'_1(x_1) \sim \delta(f'_1(x_1) - x_1) \end{aligned} \quad (21)$$

The second term:

$$\begin{aligned} & v(\{1\}) - v(\{\}) \\ &= y' \delta(f'_2(x_2) - 2x_2) \mathcal{U}(-10, 10) df'_2 dx_2 \\ &\quad - \int y' \delta(f'_1(x_1) - x_1) \mathcal{U}(-10, 10) \delta(f'_2(x_2) - 2x_2) \mathcal{U}(-10, 10) df'_1 dx_1 df'_2 dx_2 \\ &= f'_1(x_1) - 0 \\ &= f'_1(x_1) \\ &= x_1 \end{aligned} \quad (22)$$

Hence,

$$SV_1 = \frac{1}{2} (x_1 + x_1) = x_1 \quad (23)$$

Namely, $SV_1 \sim \delta(x_1)$, where δ is the Dirac function.

We can also compute the ESV for this case, which results in $\phi_1 = \mathbb{E}_{p(\varphi_1|x_1)} \{\varphi_1\} = x_1$, where $p(\varphi_1 | x_1)$ is defined by the delta-function SSV derived using the ML model: $\varphi_1 \sim \delta(x_1)$. This ESV matches the ESV computed using the DGP.

Remarks. Post-hoc explanations of ML models typically ignore the inherent randomness in the DGP, and rely on a single point estimate, while there is an entire distribution to be leveraged. We clearly see this comparing $\varphi_1 \sim \mathcal{N}\left(x_1, \frac{1}{(x_1-10)^2}\right)$ derived using the true DGP, and $\phi_1 = x_1$ derived using post-hoc explanation of the ML model. Recall that the literature primarily focuses on ESVs, which are equal in both cases.

Taking only point estimates can be misleading in various ML settings. Returning back to our original example of image classification in Sec. 1: Let's assume $x_1 = 10$ represents a blue pixel. Using post-hoc explanation of the supervised ML model output, one might think $\phi_1 = 10$ has the highest possible Shapley value (recall that $\text{supp}(x_1) \in [-10, 10]$). However, SSV shows that $\varphi_1 \sim \mathcal{N}\left(x_1, \frac{1}{(x_1-10)^2}\right)$, exhibiting high output uncertainty when $x_1 = 10$, cautioning us about the validity of this explanation. Hence, we argue that distributional inference is important for robust and trustworthy explanations.

Note that the true DGP is often unknown. The question then is: Can we derive flexible probabilistic models that can approximate the true DGP, and leverage them to infer SSV distributions?

5.2. Marginal Log-likelihood

We begin by defining $\sum_{j \in \mathcal{A}} \varphi_j^{(i)} \sim \mathcal{N}\left(\sum_{j \in \mathcal{A}} \mu_{\theta_j}(\mathbf{x}_c^{(i)}), \sum_{j \in \mathcal{A}} \sigma_{\psi_j}^2(\mathbf{x}_c^{(i)})\right)$ using $\prod_{j \in \mathcal{A}} \mathcal{N}\left(\mu_{\theta_j}(\mathbf{x}_c^{(i)}), \sigma_{\psi_j}^2(\mathbf{x}_c^{(i)})\right)$.

For a normal likelihood,

$$\int \ell_i d\Phi^{(i)} = \int \mathcal{N}\left(\phi_0 + \sum_{j \in \mathcal{A}} \varphi_j^{(i)}, \sigma^2\right) \mathcal{N}\left(\sum_{j \in \mathcal{A}} \mu_{\theta_j}(\mathbf{x}_c^{(i)}), \sum_{j \in \mathcal{A}} \sigma_{\psi_j}^2(\mathbf{x}_c^{(i)})\right) d\Phi^{(i)}, \quad (24)$$

the marginal of two normal distribution is again normal with mean:

$$\int y^{(i)} \mathcal{N}\left(\phi_0 + \sum_{j \in \mathcal{A}} \varphi_j^{(i)}, \sigma^2\right) \mathcal{N}\left(\sum_{j \in \mathcal{A}} \mu_{\theta_j}(\mathbf{x}_c^{(i)}), \sum_{j \in \mathcal{A}} \sigma_{\psi_j}^2(\mathbf{x}_c^{(i)})\right) d\Phi^{(i)} = \phi_0 + \sum_{j \in \mathcal{A}} \mu_{\theta_j}(\mathbf{x}_c^{(i)}), \quad (25)$$

and variance

$$\int y^{(i)2} \mathcal{N}\left(\phi_0 + \sum_{j \in \mathcal{A}} \varphi_j^{(i)}, \sigma^2\right) \mathcal{N}\left(\sum_{j \in \mathcal{A}} \mu_{\theta_j}(\mathbf{x}_c^{(i)}), \sum_{j \in \mathcal{A}} \sigma_{\psi_j}^2(\mathbf{x}_c^{(i)})\right) d\Phi^{(i)} - \left(\phi_0 + \sum_{j \in \mathcal{A}} \mu_{\theta_j}(\mathbf{x}_c^{(i)})\right)^2 \quad (26)$$

$$= \sigma^2 + \int \left(\sum_{j \in \mathcal{A}} \varphi_j^{(i)}\right)^2 \mathcal{N}\left(\sum_{j \in \mathcal{A}} \mu_{\theta_j}(\mathbf{x}_c^{(i)}), \sum_{j \in \mathcal{A}} \sigma_{\psi_j}^2(\mathbf{x}_c^{(i)})\right) d\Phi^{(i)} - \left(\sum_{j \in \mathcal{A}} \mu_{\theta_j}(\mathbf{x}_c^{(i)})\right)^2 \quad (27)$$

$$= \sigma^2 + \sum_{j \in \mathcal{A}} \sigma_{\psi_j}^2(\mathbf{x}_c^{(i)}). \quad (28)$$

5.3. The VSN Value Function

The expected model output is defined by the prior predictive mean i.e., $f(\mathbf{x}) = \mu_{\text{tot}}(\mathbf{x})$, hence is a natural choice for deriving ESVs. We write:

$$v(s) = \int \mu_{\text{tot}}(\mathbf{x}) p(\mathbf{x}_{\mathcal{A} \setminus s} | \mathbf{x}_s) d\mathbf{x}_{\mathcal{A} \setminus s} - \int \mu_{\text{tot}}(\mathbf{x}) p(\mathbf{x}) d\mathbf{x}. \quad (29)$$

Covert et al. (2021) showed that training models by randomly removing features independently allows for learning predictions marginalized by data conditional $p(\mathbf{x}_{\mathcal{A} \setminus s} | \mathbf{x}_s)$. Hence, $\int \mu_{\text{tot}}(\mathbf{x}) p(\mathbf{x}_{\mathcal{A} \setminus s} | \mathbf{x}_s) d\mathbf{x}_{\mathcal{A} \setminus s} = \mu_{\text{tot}}(\mathbf{x}_s)$. As such we write,

$$v(s) = \mu_{\text{tot}}(\mathbf{x}_s) - \mu_{\text{tot}}(\{\}). \quad (30)$$

Given that, for a deterministic output $\mu_{\text{tot}}(\mathbf{x}_s)$,

$$ESV_j := \sum_{s \subseteq \mathcal{C} \setminus j} p(s | \mathcal{C}) (v(s \cup j) - v(s)) \quad (31)$$

$$= \sum_{s \subseteq \mathcal{C} \setminus j} p(s | \mathcal{C}) (\mu_{\text{tot}}(\mathbf{x}_{s \cup \{j\}}) - \cancel{\mu_{\text{tot}}(\{\})} - \mu_{\text{tot}}(\mathbf{x}_{s \cup \{j\}}) + \cancel{\mu_{\text{tot}}(\{\})}) \quad (32)$$

$$= \sum_{s \subseteq \mathcal{C} \setminus j} p(s | \mathcal{C}) (v(s \cup j) - v(s)) \quad (33)$$

$$= \sum_{s \subseteq \mathcal{C} \setminus j} p(s | \mathcal{C}) (\mu_{\text{tot}}(\mathbf{x}_{s \cup \{j\}}) - \mu_{\text{tot}}(\mathbf{x}_s)). \quad (34)$$

We simply define $v_{\text{sol}}(s) = \mu_{\text{tot}}(\mathbf{x}_{s \cup \{j\}})$ and write ESV_j succinctly as:

$$\sum_{s \subseteq \mathcal{C} \setminus j} p(s | \mathcal{C}) (v_{\text{sol}}(s \cup j) - v_{\text{sol}}(s)). \quad (35)$$

5.4. Expectation of ESVs are 0

If SSVs distribute around the ESV, then we can write $\mu_{\theta_j}(\mathbf{x}_c^{(i)}) = \phi_j$, which is (following Appx. 5.3):

$$\phi_j = \sum_{s \subseteq \mathcal{C} \setminus j} p(s | \mathcal{C}) (v_{\text{sol}}(s \cup j) - v_{\text{sol}}(s)). \quad (36)$$

The value function is defined by model predictions μ_{tot} . The expected value concerning input-features:

$$\mathbb{E}_{p(\mathbf{x})} \{\phi_j\} = \int \sum_{s \subseteq \mathcal{C} \setminus j} p(s | \mathcal{C}) (v_{\text{sol}}(s \cup j) - v_{\text{sol}}(s)) p(\mathbf{x}) d\mathbf{x} \quad (37)$$

$$= \sum_{s \subseteq \mathcal{C} \setminus j} p(s | \mathcal{C}) \left(\int \mu_{\text{tot}}(\mathbf{x}_{s \cup \{j\}}) p(\mathbf{x}) d\mathbf{x} - \int \mu_{\text{tot}}(\mathbf{x}_s) p(\mathbf{x}) d\mathbf{x} \right) \quad (38)$$

$$= \sum_{s \subseteq \mathcal{C} \setminus j} p(s | \mathcal{C}) (\mu_{\text{tot}}(\{\}) - \mu_{\text{tot}}(\{\})) \quad (39)$$

$$= 0 \quad (40)$$

In practice, we do not have access to $p(\mathbf{x})$. Hence, we approximate it using the empirical data distribution. In this paper, we use *held out* validation sets when generating Fig. 2 to demonstrate VSN's generalizability.

5.5. Variational Bound

In variational methods, we minimize the KL-divergence distance between two distributions. In our case, a variational *solution* posterior $q_{\text{sol}}(\Phi^{(i)} | \mathbf{x}_c^{(i)}) = \prod_{j \in \mathcal{A}} q_{\text{sol}}(\varphi_j^{(i)} | \mathbf{x}_c^{(i)})$ and model posterior $p(\Phi^{(i)} | \mathbf{x}_c^{(i)}, y^{(i)})$:

$$\min D_{\text{KL}} \left(\prod_{i=1}^N q_{\text{sol}}(\Phi^{(i)} | \mathbf{x}_c^{(i)}) \parallel \prod_{i=1}^N p(\Phi^{(i)} | \mathbf{x}_c^{(i)}, y^{(i)}) \right) \quad (41)$$

$$\min \mathbb{E}_{\prod_{i=1}^N q_{\text{sol}}(\Phi^{(i)} | \mathbf{x}_c^{(i)})} \left\{ \log \prod_{i=1}^N q_{\text{sol}}(\Phi^{(i)} | \mathbf{x}_c^{(i)}) - \log \prod_{i=1}^N p(\Phi^{(i)} | \mathbf{x}_c^{(i)}, y^{(i)}) \right\} \quad (42)$$

$$\min \sum_{i=1}^N \mathbb{E}_{q_{\text{sol}}(\Phi^{(i)} | \mathbf{x}_c^{(i)})} \{ \log q_{\text{sol}}(\Phi^{(i)} | \mathbf{x}_c^{(i)}) - \log p(\Phi^{(i)} | \mathbf{x}_c^{(i)}, y^{(i)}) \} \quad (43)$$

$$\min \sum_{i=1}^N \mathbb{E}_{q_{\text{sol}}(\Phi^{(i)} | \mathbf{x}_c^{(i)})} \left\{ \log q_{\text{sol}}(\Phi^{(i)} | \mathbf{x}_c^{(i)}) - \log \frac{p(\Phi^{(i)} | \mathbf{x}_c^{(i)}) p(y^{(i)} | \Phi^{(i)})}{p(y^{(i)} | \mathbf{x}_c^{(i)})} \right\} \quad (44)$$

$$\min \sum_{i=1}^N \mathbb{E}_{q_{\text{sol}}(\Phi^{(i)} | \mathbf{x}_c^{(i)})} \{ \log q_{\text{sol}}(\Phi^{(i)} | \mathbf{x}_c^{(i)}) - \log p(\Phi^{(i)} | \mathbf{x}_c^{(i)}) p(y^{(i)} | \Phi^{(i)}) \} - \sum_{i=1}^N \log p(y^{(i)} | \mathbf{x}_c^{(i)}) \quad (45)$$

Therefore, we

$$\max \sum_{i=1}^N \mathbb{E}_{q_{\text{sol}}(\Phi^{(i)} | \mathbf{x}_c^{(i)})} \{ \log p(y^{(i)} | \Phi^{(i)}) \} - \underbrace{\sum_{i=1}^N D_{\text{KL}}(q_{\text{sol}}(\Phi^{(i)} | \mathbf{x}_c^{(i)}) \parallel p(\Phi^{(i)} | \mathbf{x}_c^{(i)}))}_{\mathcal{R}} \leq \underbrace{\sum_{i=1}^N \log p(y^{(i)} | \mathbf{x}_c^{(i)})}_{\mathcal{L}} \quad (46)$$

$$\max \sum_{i=1}^N \mathbb{E}_{q_{\text{sol}}(\Phi^{(i)} | \mathbf{x}_c^{(i)})} \{ \log p(y^{(i)} | \Phi^{(i)}) \} - \mathcal{R} \leq \mathcal{L} \quad (47)$$

5.6. Interchanging Expected Values

We first use the efficiency property of Shapley values, and the design choice of equivalence of variances between posterior and prior, to derive

$$q_{\text{so1}} \left(\sum_{j \in \mathcal{A}} \varphi_j^{(i)} \mid \mathbf{x}_c^{(i)} \right) = \mathcal{N} \left(\sum_{j \in \mathcal{A}} \mu_{\theta_j}(\mathbf{x}_c^{(i)}), \sum_{j \in \mathcal{A}} \sigma_{\psi_j}^2(\mathbf{x}_c^{(i)}) \right), \quad (48)$$

$$= \mathcal{N} \left(\mu_{\text{tot}}(\mathbf{x}_c^{(i)}) - \phi_0, \sum_{j \in \mathcal{A}} \sigma_{\psi_j}^2(\mathbf{x}_c^{(i)}) \right), \quad (49)$$

$$= p \left(\sum_{j \in \mathcal{A}} \varphi_j^{(i)} \mid \mathbf{x}_c^{(i)} \right) \quad (50)$$

Now, we can derive

$$\mathbb{E}_{q_{\text{so1}}(\Phi^{(i)} \mid \mathbf{x}^{(i)})} \left\{ \log f \left(\phi_0 + \sum_{j \in \mathcal{A}} \varphi_j^{(i)} \right) \right\} = \mathbb{E}_{q_{\text{so1}}(\sum_{j \in \mathcal{A}} \varphi_j^{(i)} \mid \mathbf{x}^{(i)})} \left\{ \log f \left(\phi_0 + \sum_{j \in \mathcal{A}} \varphi_j^{(i)} \right) \right\} \quad (51)$$

$$= \mathbb{E}_{p(\sum_{j \in \mathcal{A}} \varphi_j^{(i)} \mid \mathbf{x}^{(i)})} \left\{ \log f \left(\phi_0 + \sum_{j \in \mathcal{A}} \varphi_j^{(i)} \right) \right\} \quad (52)$$

$$= \mathbb{E}_{p(\Phi^{(i)} \mid \mathbf{x}^{(i)})} \left\{ \log f \left(\phi_0 + \sum_{j \in \mathcal{A}} \varphi_j^{(i)} \right) \right\} \quad \square \quad (53)$$

5.7. Deriving a Tighter Lower-bound

Since log is a concave function we know that

$$\mathbb{E}_{p(\Phi^{(i)} \mid \mathbf{x}^{(i)})} \left\{ \log f \left(\phi_0 + \sum_{j \in \mathcal{A}} \varphi_j^{(i)} \right) \right\} \leq \log \mathbb{E}_{p(\Phi^{(i)} \mid \mathbf{x}^{(i)})} \left\{ f \left(\phi_0 + \sum_{j \in \mathcal{A}} \varphi_j^{(i)} \right) \right\}. \quad (54)$$

Since $\mathcal{R} \geq 0$,

$$\sum_{i=1}^N \mathbb{E}_{p(\Phi^{(i)} \mid \mathbf{x}^{(i)})} \{ \log p(y^{(i)} \mid \Phi^{(i)}) \} - \mathcal{R} \leq \sum_{i=1}^N \log \mathbb{E}_{p(\Phi^{(i)} \mid \mathbf{x}^{(i)})} \{ p(y^{(i)} \mid \Phi^{(i)}) \} - \mathcal{R} \leq \mathcal{L}, \quad (55)$$

Note that, since $\sum_{i=1}^N \log \mathbb{E}_{p(\Phi^{(i)} \mid \mathbf{x}^{(i)})} \{ p(y^{(i)} \mid \Phi^{(i)}) \} = \mathcal{L}$, we can scale \mathcal{R} with $b \geq 0$. Therefore, the final loss we maximize is

$$\mathcal{V} = \mathcal{L} - b \mathcal{R}, \quad (56)$$

To ensure Inequality 55, we use $0 \leq b \leq 1$.

5.8. Unbiased Surrogate Regularization Function

To show that our surrogate regularizer is unbiased we take the expected value of its gradients with respect to Θ :

$$\mathbb{E}_{\mathcal{U}(1,d)} \left\{ \mathbb{E}_{p(s|\mathcal{C})} \left\{ \mathbb{E}_{p(s|\mathcal{C})} \left\{ \nabla_{\theta_{j(i)}} d \frac{\Delta_{ij(i)}(\hat{s}) \Delta_{ij(i)}(\hat{s})}{2\sigma_{\psi_{j(i)}}^2(\mathbf{x}_c^{(i)})} \right\} \right\} \right\} \quad (57)$$

Since $\hat{s} \perp\!\!\!\perp \hat{s}$

$$= \mathbb{E}_{\mathcal{U}(1,d)} \left\{ d \frac{\nabla_{\theta_{j(i)}} \mathbb{E}_{p(s|\mathcal{C})} \{ \Delta_{ij(i)}(\hat{s}) \} \mathbb{E}_{p(s|\mathcal{C})} \{ \Delta_{ij(i)}(\hat{s}) \}}{2\sigma_{\psi_{j(i)}}^2(\mathbf{x}_c^{(i)})} \right\} \quad (58)$$

Since the gradients of $\Delta_{ij(i)}(\hat{s})$ are detached

$$= \mathbb{E}_{\mathcal{U}(1,d)} \left\{ d \frac{(\nabla_{\theta_{j(i)}} \mathbb{E}_{p(s|\mathcal{C})} \{ \hat{\mu}_{\text{sol}_{j(i)}}(\mathbf{x}_c^{(i)}, \hat{s}) \} - \nabla_{\theta_{j(i)}} \mu_{\theta_{j(i)}}(\mathbf{x}_c^{(i)}) (\mathbb{E}_{p(s|\mathcal{C})} \{ \hat{\mu}_{\text{sol}_{j(i)}}(\mathbf{x}_c^{(i)}, \hat{s}) \} - \mu_{\theta_{j(i)}}(\mathbf{x}_c^{(i)})))}{2\sigma_{\psi_{j(i)}}^2(\mathbf{x}_c^{(i)})} \right\} \quad (59)$$

Since $\mathbb{E}_{p(s|\mathcal{C})} \{ \hat{\mu}_{\text{sol}_{j(i)}}(\mathbf{x}_c^{(i)}, \hat{s}) \} = \mu_{\text{sol}_{j(i)}}(\mathbf{x}_c^{(i)})$

$$= \mathbb{E}_{\mathcal{U}(1,d)} \left\{ d \frac{(\nabla_{\theta_{j(i)}} \mu_{\text{sol}_{j(i)}}(\mathbf{x}_c^{(i)}) - \nabla_{\theta_{j(i)}} \mu_{\theta_{j(i)}}(\mathbf{x}_c^{(i)})) (\mu_{\text{sol}_{j(i)}}(\mathbf{x}_c^{(i)}) - \mu_{\theta_{j(i)}}(\mathbf{x}_c^{(i)}))}{2\sigma_{\psi_{j(i)}}^2(\mathbf{x}_c^{(i)})} \right\} \quad (60)$$

$$= d \sum_{j(i) \in \mathcal{A}} \frac{1}{d} \nabla_{\theta_{j(i)}} D_{\text{KL}}(q_{\text{sol}}(\phi_{j(i)} | \mathbf{x}_c^{(i)}) \| p(\phi_{j(i)} | \mathbf{x}_c^{(i)})) \quad (61)$$

$$= \sum_{j \in \mathcal{A}} \nabla_{\theta_j} D_{\text{KL}}(q_{\text{sol}}(\phi_j | \mathbf{x}_c^{(i)}) \| p(\phi_j | \mathbf{x}_c^{(i)})) \quad (62)$$

Therefore, our surrogate regularization function yields unbiased gradients with respect to θ_j .

Note that ∇_{ϕ_0} has the same steps as above. Moving forward, we calculate the expected gradients of $\psi_{j(i)}$:

$$\mathbb{E}_{\mathcal{U}(1,d)} \left\{ \mathbb{E}_{p(s|\mathcal{C})} \left\{ \mathbb{E}_{p(s|\mathcal{C})} \left\{ \nabla_{\psi_{j(i)}} d \frac{\Delta_{ij(i)}(\hat{s}) \Delta_{ij(i)}(\hat{s})}{2\sigma_{\psi_{j(i)}}^2(\mathbf{x}_c^{(i)})} \right\} \right\} \right\} \quad (63)$$

$$= \mathbb{E}_{\mathcal{U}(1,d)} \left\{ \nabla_{\psi_{j(i)}} d \frac{\mathbb{E}_{p(s|\mathcal{C})} \{ \Delta_{ij(i)}(\hat{s}) \} \mathbb{E}_{p(s|\mathcal{C})} \{ \Delta_{ij(i)}(\hat{s}) \}}{2\sigma_{\psi_{j(i)}}^2(\mathbf{x}_c^{(i)})} \right\} \quad (64)$$

$$= \mathbb{E}_{\mathcal{U}(1,d)} \left\{ d \frac{(\mathbb{E}_{p(s|\mathcal{C})} \{ \hat{\mu}_{\text{sol}_{j(i)}}(\mathbf{x}_c^{(i)}, \hat{s}) \} - \mu_{\theta_{j(i)}}(\mathbf{x}_c^{(i)})) (\mathbb{E}_{p(s|\mathcal{C})} \{ \hat{\mu}_{\text{sol}_{j(i)}}(\mathbf{x}_c^{(i)}, \hat{s}) \} - \mu_{\theta_{j(i)}}(\mathbf{x}_c^{(i)}))}{2\sigma_{\psi_{j(i)}}^2(\mathbf{x}_c^{(i)})} \right\} \quad (65)$$

$$= \mathbb{E}_{\mathcal{U}(1,d)} \left\{ \nabla_{\psi_{j(i)}} d \frac{(\mu_{\text{sol}_{j(i)}}(\mathbf{x}_c^{(i)}) - \mu_{\theta_{j(i)}}(\mathbf{x}_c^{(i)}))^2}{2\sigma_{\psi_{j(i)}}^2(\mathbf{x}_c^{(i)})} \right\} \quad (66)$$

$$= d \sum_{j(i) \in \mathcal{A}} \frac{1}{d} \nabla_{\psi_{j(i)}} D_{\text{KL}}(q_{\text{sol}}(\phi_{j(i)} | \mathbf{x}_c^{(i)}) \| p(\phi_{j(i)} | \mathbf{x}_c^{(i)})) \quad (67)$$

$$= \sum_{j \in \mathcal{A}} \nabla_{\psi_j} D_{\text{KL}}(q_{\text{sol}}(\phi_j | \mathbf{x}_c^{(i)}) \| p(\phi_j | \mathbf{x}_c^{(i)})) \quad (68)$$

Therefore, our surrogate regularization function yields unbiased gradients with respect to ψ_j .

Since our surrogate function gives unbiased gradients for θ_j , ψ_j and ϕ_0 , our surrogate function is unbiased for the gradients ∇_{Θ} . \square

5.9. Masking Operations Example

In this section, we demonstrate example masking matrices and operations. For illustrative purposes, we use a 4 layer neural network with hidden dimensions [3, 10, 10, 10, 6]. We begin by defining our initial masking matrix M_1 as described in Sec. 2.5:

$$M_1 = \begin{bmatrix} 1 & 1 & 1 & 0 & 0 & 0 & 0 & 0 & 0 & 0 \\ 0 & 0 & 0 & 1 & 1 & 1 & 0 & 0 & 0 & 0 \\ 0 & 0 & 0 & 0 & 0 & 0 & 1 & 1 & 1 & 1 \end{bmatrix}$$

Moving forward, we define the intermediate masking matrices M_k by repeating the rows of $M_{1:k-1}$ as described at the end of Sec. 2.5 in the main manuscript:

$$M_2 = \begin{bmatrix} 1 & 1 & 1 & 0 & 0 & 0 & 0 & 0 & 0 & 0 \\ 1 & 1 & 1 & 0 & 0 & 0 & 0 & 0 & 0 & 0 \\ 1 & 1 & 1 & 0 & 0 & 0 & 0 & 0 & 0 & 0 \\ 0 & 0 & 0 & 1 & 1 & 1 & 0 & 0 & 0 & 0 \\ 0 & 0 & 0 & 1 & 1 & 1 & 0 & 0 & 0 & 0 \\ 0 & 0 & 0 & 1 & 1 & 1 & 0 & 0 & 0 & 0 \\ 0 & 0 & 0 & 0 & 0 & 0 & 1 & 1 & 1 & 1 \\ 0 & 0 & 0 & 0 & 0 & 0 & 1 & 1 & 1 & 1 \\ 0 & 0 & 0 & 0 & 0 & 0 & 1 & 1 & 1 & 1 \\ 0 & 0 & 0 & 0 & 0 & 0 & 1 & 1 & 1 & 1 \end{bmatrix}$$

$$M_3 = \begin{bmatrix} 1 & 1 & 1 & 0 & 0 & 0 & 0 & 0 & 0 & 0 \\ 1 & 1 & 1 & 0 & 0 & 0 & 0 & 0 & 0 & 0 \\ 1 & 1 & 1 & 0 & 0 & 0 & 0 & 0 & 0 & 0 \\ 0 & 0 & 0 & 1 & 1 & 1 & 0 & 0 & 0 & 0 \\ 0 & 0 & 0 & 1 & 1 & 1 & 0 & 0 & 0 & 0 \\ 0 & 0 & 0 & 1 & 1 & 1 & 0 & 0 & 0 & 0 \\ 0 & 0 & 0 & 0 & 0 & 0 & 1 & 1 & 1 & 1 \\ 0 & 0 & 0 & 0 & 0 & 0 & 1 & 1 & 1 & 1 \\ 0 & 0 & 0 & 0 & 0 & 0 & 1 & 1 & 1 & 1 \\ 0 & 0 & 0 & 0 & 0 & 0 & 1 & 1 & 1 & 1 \end{bmatrix}$$

and

$$M_4 = \begin{bmatrix} 1 & 1 & 0 & 0 & 0 & 0 \\ 1 & 1 & 0 & 0 & 0 & 0 \\ 1 & 1 & 0 & 0 & 0 & 0 \\ 0 & 0 & 1 & 1 & 0 & 0 \\ 0 & 0 & 1 & 1 & 0 & 0 \\ 0 & 0 & 1 & 1 & 0 & 0 \\ 0 & 0 & 0 & 0 & 1 & 1 \\ 0 & 0 & 0 & 0 & 1 & 1 \\ 0 & 0 & 0 & 0 & 1 & 1 \\ 0 & 0 & 0 & 0 & 1 & 1 \end{bmatrix}$$

Now we compute the following matrix multiplication with non-zero elements of $M_{1:k}$ denoting the information flow until layer k (Germain et al., 2015):

$$M_{1:2} = \begin{bmatrix} 3 & 3 & 3 & 0 & 0 & 0 & 0 & 0 & 0 & 0 \\ 0 & 0 & 0 & 3 & 3 & 3 & 0 & 0 & 0 & 0 \\ 0 & 0 & 0 & 0 & 0 & 0 & 4 & 4 & 4 & 4 \end{bmatrix}$$

Notice that the columns of M_3 have been constructed by repeating the rows of $M_{1:2}$ (compare) as described in the main manuscript. We now compute $M_{1:3}$:

$$M_{1:3} = \begin{bmatrix} 9 & 9 & 9 & 0 & 0 & 0 & 0 & 0 & 0 & 0 \\ 0 & 0 & 0 & 9 & 9 & 9 & 0 & 0 & 0 & 0 \\ 0 & 0 & 0 & 0 & 0 & 0 & 16 & 16 & 16 & 16 \end{bmatrix}$$

Notice that the columns of M_4 has been constructed by repeating the rows of $M_{1:3}$. Observe that M_4 distributes 2 embedding dimensions per feature:

$$\begin{aligned}
 M_{1:4} &= \begin{bmatrix} 27 & 27 & 0 & 0 & 0 & 0 \\ 0 & 0 & 27 & 27 & 0 & 0 \\ 0 & 0 & 0 & 0 & 64 & 64 \end{bmatrix} \\
 &= \begin{bmatrix} \gamma_1 & \gamma_1 & 0 & 0 & 0 & 0 \\ 0 & 0 & \gamma_2 & \gamma_2 & 0 & 0 \\ 0 & 0 & 0 & 0 & \gamma_3 & \gamma_3 \end{bmatrix}
 \end{aligned}$$

Notice that $M_{1:4}$ allows for creating two dimensional embeddings as it permits information flow to two disjoint output neurons for each input feature (i.e., outputs one and two only depend on x_1 , outputs three and four only depend on x_2 , and so forth).

γ_i values depend on how the 1s are distributed in masking matrices; an equal distribution would result in more uniform γ_i values. In practice, instead of using a single $\text{rint}(\cdot)$ function, we choose to round up or down, randomly. An example of such a method is also illustrated below:

We first define the initial masking matrix as follows

$$M_1 = \begin{bmatrix} 1 & 1 & 1 & 1 & 1 & 0 & 0 & 0 & 0 & 0 \\ 0 & 0 & 0 & 0 & 0 & 1 & 1 & 1 & 0 & 0 \\ 0 & 0 & 0 & 0 & 0 & 0 & 0 & 0 & 1 & 1 \end{bmatrix}$$

We then define M_k for $k > 1$

$$M_2 = \begin{bmatrix} 1 & 1 & 1 & 0 & 0 & 0 & 0 & 0 & 0 & 0 \\ 1 & 1 & 1 & 0 & 0 & 0 & 0 & 0 & 0 & 0 \\ 1 & 1 & 1 & 0 & 0 & 0 & 0 & 0 & 0 & 0 \\ 1 & 1 & 1 & 0 & 0 & 0 & 0 & 0 & 0 & 0 \\ 1 & 1 & 1 & 0 & 0 & 0 & 0 & 0 & 0 & 0 \\ 0 & 0 & 0 & 1 & 1 & 1 & 1 & 0 & 0 & 0 \\ 0 & 0 & 0 & 1 & 1 & 1 & 1 & 0 & 0 & 0 \\ 0 & 0 & 0 & 1 & 1 & 1 & 1 & 0 & 0 & 0 \\ 0 & 0 & 0 & 0 & 0 & 0 & 0 & 1 & 1 & 1 \\ 0 & 0 & 0 & 0 & 0 & 0 & 0 & 1 & 1 & 1 \end{bmatrix}$$

$$M_3 = \begin{bmatrix} 1 & 1 & 1 & 1 & 0 & 0 & 0 & 0 & 0 & 0 \\ 1 & 1 & 1 & 1 & 0 & 0 & 0 & 0 & 0 & 0 \\ 1 & 1 & 1 & 1 & 0 & 0 & 0 & 0 & 0 & 0 \\ 0 & 0 & 0 & 0 & 1 & 1 & 1 & 1 & 0 & 0 \\ 0 & 0 & 0 & 0 & 1 & 1 & 1 & 1 & 0 & 0 \\ 0 & 0 & 0 & 0 & 1 & 1 & 1 & 1 & 0 & 0 \\ 0 & 0 & 0 & 0 & 1 & 1 & 1 & 1 & 0 & 0 \\ 0 & 0 & 0 & 0 & 0 & 0 & 0 & 0 & 1 & 1 \\ 0 & 0 & 0 & 0 & 0 & 0 & 0 & 0 & 1 & 1 \\ 0 & 0 & 0 & 0 & 0 & 0 & 0 & 0 & 1 & 1 \end{bmatrix}$$

$$M_4 = \begin{bmatrix} 1 & 1 & 0 & 0 & 0 & 0 \\ 1 & 1 & 0 & 0 & 0 & 0 \\ 1 & 1 & 0 & 0 & 0 & 0 \\ 1 & 1 & 0 & 0 & 0 & 0 \\ 0 & 0 & 1 & 1 & 0 & 0 \\ 0 & 0 & 1 & 1 & 0 & 0 \\ 0 & 0 & 1 & 1 & 0 & 0 \\ 0 & 0 & 1 & 1 & 0 & 0 \\ 0 & 0 & 0 & 0 & 1 & 1 \\ 0 & 0 & 0 & 0 & 1 & 1 \end{bmatrix}$$

Finally, we confirm that the mask multiplications result in desired information flow

$$\begin{aligned}
M_{1:2} &= \begin{bmatrix} 5 & 5 & 5 & 0 & 0 & 0 & 0 & 0 & 0 & 0 \\ 0 & 0 & 0 & 3 & 3 & 3 & 3 & 0 & 0 & 0 \\ 0 & 0 & 0 & 0 & 0 & 0 & 0 & 2 & 2 & 2 \end{bmatrix} \\
M_{1:3} &= \begin{bmatrix} 15 & 15 & 15 & 15 & 0 & 0 & 0 & 0 & 0 & 0 \\ 0 & 0 & 0 & 0 & 12 & 12 & 12 & 12 & 0 & 0 \\ 0 & 0 & 0 & 0 & 0 & 0 & 0 & 0 & 6 & 6 \end{bmatrix} \\
M_{1:4} &= \begin{bmatrix} 60 & 60 & 0 & 0 & 0 & 0 \\ 0 & 0 & 48 & 48 & 0 & 0 \\ 0 & 0 & 0 & 0 & 12 & 12 \end{bmatrix} \\
&= \begin{bmatrix} \gamma_1 & \gamma_1 & 0 & 0 & 0 & 0 \\ 0 & 0 & \gamma_2 & \gamma_2 & 0 & 0 \\ 0 & 0 & 0 & 0 & \gamma_3 & \gamma_3 \end{bmatrix}
\end{aligned}$$

5.10. Distance Measures

In this section, we describe our approach to measure the distance between the marginals (namely, $p(y, \mathbf{x}_s)$) of our novel masked network architecture and feedforward architecture with marginalization (missingness) indicators, ξ .

5.10.1. JENSEN-SHANNON DIVERGENCE

The metric that we are interested in is $\frac{1}{|\mathcal{A}|} \sum_{j \in \mathcal{A}} \sum_{s \in \mathcal{A} \setminus \{j\}} p(s | \mathcal{A}) \text{JSD}(\text{Model Marginals}, \text{Empirical Marginals})$, which calculates the distance between marginals for every possible coalition can be made for any given feature j weighted according to its Shapley value weights that are used during Shapley value calculations. This allows for arriving at a single metric calculated by weighting the distance between ground truth marginals and model marginals by their occurrence in Shapley value calculations. We follow the below steps.

Define $dist = 0$.

For every feature $j \in \mathcal{A}$ and $s \in \mathcal{A} \setminus \{j\}$:

1. **Empirical sampling:** Sample $[\mathbf{y}, \mathbf{X}] \sim \hat{p}(\mathbf{y}, \mathbf{X})$ from empirical joint.
2. **Empirical marginals:** Remove the columns $k \notin s$ from $[\mathbf{y}, \mathbf{X}]$ to obtain empirical marginals $[\mathbf{y}, \mathbf{X}_s]$.
3. **Sample from model marginals:** Sample $\hat{\mathbf{y}} \sim p(\mathbf{y} | \mathbf{X}_s)$ from model using masked and/or vanilla network and define $[\hat{\mathbf{y}}, \mathbf{X}_s]$ as model marginal samples.
4. **Measure distance:** Compute $dist = dist + \frac{1}{|\mathcal{A}|} p(s | \mathcal{A} \setminus \{j\}) \text{JSD}(p([\mathbf{y}, \mathbf{X}_s]), p([\hat{\mathbf{y}}, \mathbf{X}_s]))$.

Computing $\text{JSD}(p([\mathbf{y}, \mathbf{X}_s]), p([\hat{\mathbf{y}}, \mathbf{X}_s]))$. In order to measure the JS-Divergence between two samples, we arrive at $p([\mathbf{y}, \mathbf{X}_s])$ and $p([\hat{\mathbf{y}}, \mathbf{X}_s])$ discretizing the empirical distribution by fitting a histogram of different bin sizes to both $[\mathbf{y}, \mathbf{X}]$ and $[\hat{\mathbf{y}}, \mathbf{X}_s]$. Given such a discretized (multinomial) distribution, JS-Divergence has a closed-form solution and can be computed easily. We apply this for various bin sizes by sampling 20 bin sizes from $U(10, 200)$. We take the average, which gives a single number, to approximate JS-Divergence metric.

The error bars in Fig. 3 are generated by applying the above procedure to 5 different models trained of different train-test split sets (5 fold cross-validation).

5.10.2. WASSERSTEIN DISTANCE

We follow the same procedure described in Appx. 5.10.1, with a modification on Step 4 where we use $\text{WD}(\cdot, \cdot)$ instead of $\text{JSD}(\cdot, \cdot)$. We use POT: Python Optimal Transport software package to calculate the Wasserstein Distance between two empirical samples and refer reader to (Flamary et al., 2021) for details.

5.10.3. COMPARISON TO VANILLA NETWORK WITHOUT MISSINGNESS INDICATORS (ξ)

In Fig. 5, we compare the quality of marginals of our masked approach and vanilla approach without missingness indicators (ξ) as inputs. As expected, the vanilla network without ξ as input performs worse than the vanilla network with ξ as input.

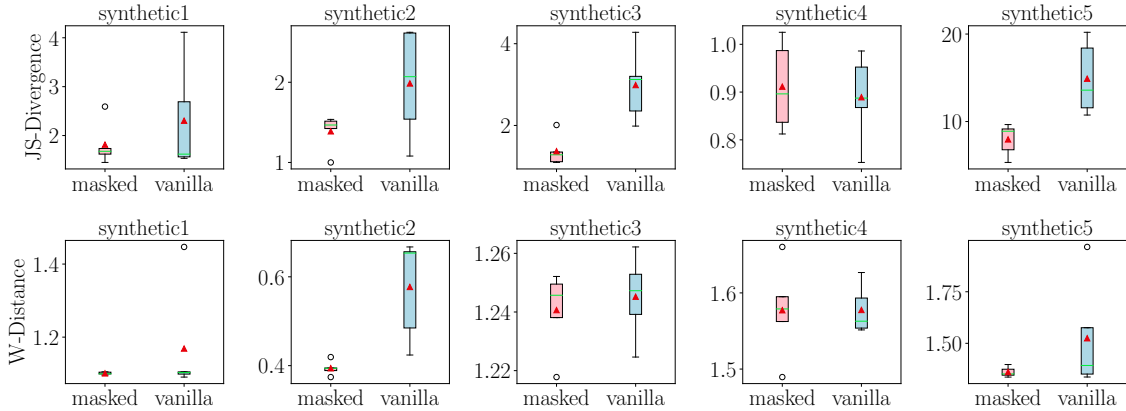


Figure 5. Distance of VSN’s marginals to the empirical data samples: comparison of the proposed masked approach and a feedforward approach with baseline replacement without missingness indicators as inputs to vanilla network. \blacktriangle represents the mean and \blacksquare represents the median fold results. Error bars denote the 1.5 interquartile range.

5.11. Experimental Setup: Baselines Models, Datasets and Hyperparameter selection

In this section we describe the datasets and baseline models used in our experiments, as well as the hyperparameter selection procedure used.

5.11.1. REAL-WORLD DATASETS

Regression Datasets. Below, we describe the datasets used for classification task:

1. **Parkinsons telemonitoring (PKSN):** The dataset features voice data from 42 Parkinson’s patients in the early stages, captured over six months using a telemonitoring device for distant symptom monitoring. These autonomous recordings, taken at their homes, total 5875 data points. The task is to predict Clinician’s motor UPDRS score (Tsanas et al., 2009).
2. **Medical expenses (MED):** 1,338 patients from United States (Lantz, 2019). The task is to predict medical expenses. Here, the unit of measurement is United States Dollars (USD).
3. **Bike sharing (BIKE):** The dataset of 17,389 entries aims to predict total bike rentals, covering both casual and registered users (Fanaee-T, 2013).
4. **Pumadyn (PUMA):** The dataset, derived from a simulated Unimation Puma 560 robot arm’s dynamics, comprises 8,192 instances (Ghahramani, 1996).
5. **Greenhouse gas observing network (GAS):** The dataset features time series of greenhouse gas concentrations across 2,921 grid cells in California, generated using the WRF-Chem simulation model. The goal is to predict the green house gas concentration (Lucas, 2015).
6. **Wine quality (WINE):** 1599 red wine instances. The task is to predict wine quality (Cortez et al., 2009).
7. **Elevators (ELEV):** This dataset is derived from the F-16 aircraft control task predicting the status of aircraft elevators.

Classification Datasets. Below, we describe the datasets used for classification task:

1. **Heloc (FICO):** 9,861 credit applications (FICO, 2018). The task is to classify risk performance. The good risk performance is represented by 1.

2. **Spambase (SPAM):** The classification task involves 4601 instances aimed at determining whether a given email is classified as spam or not (Hopkins et al., 1999). Spam emails are represented by 1.
3. **Intensive care unit (ICU):** 15,830 intensive care unit (ICU) cases from Argentina, Australia, New Zealand, Sri Lanka, Brazil, and United States (Goldberger et al., 2000; Meredith et al., 2020). The task is to classify ICU mortality. The ICU mortality is represented by 1.
4. **Census income (CENS):** Demographic (such as age, education etc.) information of 48,842 people. The task is to predict if the person earns more than 50,000 USD a year (Kohavi, 1996). Income of more than 50,000 USD a year is represented by 1.

5.1.1.2. SIMULATED DATASETS

In this section we describe the data generating processes of the simulated datasets. We employ non-trivial functions with heteroscedastic noise and complex interactions. We generate 8000 examples for each synthetic dataset.

Synthetic1. DGP is as described in Sec. 3.4: (i) Draw $x_1^{(i)}, x_2^{(i)}, x_3^{(i)} \sim U(-4, 4)$, (ii) Draw $f_1^{(i)} \sim \mathcal{N}\left(2 + \exp\{-x_1^{(i)2}\}, 0.6 \cos(0.03x_1^{(i)})^{800}\right)$, $f_2^{(i)} \sim \mathcal{N}\left(1 + \sin(-x_2^{(i)2}), 0.2|x_2^{(i)}|\right)$, and $f_3^{(i)} = 3 \cos(3x_3^{(i)}) + 4 \sin(5x_3^{(i)})$, (iii) Calculate $y^{(i)} = f_1^{(i)} + f_2^{(i)} + f_3^{(i)}$.

Synthetic2. (i) Draw $x_1^{(i)}, x_2^{(i)}, x_3^{(i)} \sim U(-4, 4)$, (ii) Calculate $f_1^{(i)} = \exp\{-x_1^{(i)2}\} x_1^{(i)}$, $f_2^{(i)} = 0.5x_2^{(i)} \sin(x_2^{(i)})$, $f_3^{(i)} = \cos(3x_3^{(i)}) \sin(x_3^{(i)})$, (iii) Calculate $y^{(i)} = f_1^{(i)} + f_2^{(i)} + f_3^{(i)}$.

Synthetic3. (i) Draw $x_1^{(i)}, x_2^{(i)}, x_3^{(i)} \sim U(-4, 4)$, (ii) Calculate $f_1^{(i)} = 4 \sin(x_1^{(i)}) + 2 \sin(2x_1^{(i)})$, $f_2^{(i)} = 3 \cos(3x_2^{(i)}) \sin(5x_2^{(i)})$, $f_3^{(i)} = \cos(2x_3^{(i)}) + x_3^{(i)2}/7$, $f_{12}^{(i)} = \exp\{-(x_1^{(i)} + x_2^{(i)})^2\}$, $f_{13}^{(i)} = (x_1^{(i)} - 3)x_3^{(i)} \sin(x_1^{(i)}) \cos(x_3^{(i)})/2$, $f_{23}^{(i)} = x_2^{(i)}x_3^{(i)}/2$, (iii) Draw $y^{(i)} \sim \mathcal{N}(f_1^{(i)} + f_2^{(i)} + f_3^{(i)} + f_{12}^{(i)} + f_{13}^{(i)} + f_{23}^{(i)}, 0.01)$.

Synthetic4. (i) Draw $x_1^{(i)}, x_2^{(i)}, x_3^{(i)} \sim U(-4, 4)$, (ii) Calculate $f_1^{(i)} = \exp\{-1/x_1^{(i)2}\} + \sin(100/x_1^{(i)})$, $f_2^{(i)} = \exp\{-|\cos(|x_2^{(i)}|) + 1/2 \sin(2x_2^{(i)})|\} + x_2^{(i)}/4$, $f_3^{(i)} = \tanh(x_3^{(i)2})$, $f_{12}^{(i)} = \sin(x_1^{(i)2} + x_2^{(i)2})/2$, (iii) Calculate $y^{(i)} = f_1^{(i)} + f_2^{(i)} + f_3^{(i)} + f_{12}^{(i)}$.

Synthetic5. (i) Draw $x_1^{(i)}, x_2^{(i)}, x_3^{(i)} \sim U(-4, 4)$, (ii) Calculate $f_1^{(i)} = |x_1^{(i)}|/10 + x_1^{(i)2}/10 + \sin(x_1^{(i)})$, $f_2^{(i)} = \cos(5x_2^{(i)}) + \sin(2x_2^{(i)}) + x_2^{(i)}$, $f_3^{(i)} = \exp\{-x_3^{(i)100}\}$, $f_{12}^{(i)} = 5(x_1^{(i)10} + x_2^{(i)10})^{1/10}/2$, $f_{23}^{(i)} = 5|\sin(x_3^{(i)}x_2^{(i)}) \cos(x_3^{(i)}x_2^{(i)})|/2$, (iii) Draw $y^{(i)} \sim \mathcal{N}(f_1^{(i)} + f_2^{(i)} + f_3^{(i)} + f_{12}^{(i)}, 0.01)$.

The observed data are only $\{\mathbf{x}^{(i)}, y^{(i)}\}_{i=1}^N$ pairs for all simulated datasets.

5.1.1.3. BASELINE MODELS

1. **Bayesian Linear/Logistic Regression (LIN):** The simplest, yet the most explainable model. Linear models quantify the feature importance and feature importance uncertainty through the model coefficients. We use Bayesian linear regression for regression and Bayesian logistic regression for classification tasks. We use the implementation by Pedregosa et al. (2011).
2. **Explainable Boosting Machines (EBM):** The state-of-the-art explainable additive model which uses an ensemble shallow trees with boosting to model each component (Lou et al., 2013; Caruana et al., 2015). We use the implementation by Nori et al. (2019).
3. **Random Forest (RF):** Another ensemble learning algorithm that RFs by building multiple trees independently using bagging, and averaging the predictions of each individual tree. We use the implementation by Pedregosa et al. (2011).
4. **Light Gradient Boosting Machines (LGBM):** LGBM uses a leaf-wise growth strategy, prioritizing splits that result in the largest decrease in loss, whereas most traditional tree-based algorithms grow trees level-wise. While leaf-wise growth can achieve better accuracy, it might also lead to overfitting, especially on smaller datasets. Thus, careful hyperparameter tuning, including regularization, is essential when using LGBM (Ke et al., 2017).

5. **Gradient Boosted Trees (XGB):** A well-known ensemble learning algorithm that combines several weak learners. In particular, each weak learner is trained to improve the ensemble performance, one at a time. We use the implementation by [Chen & Guestrin \(2016\)](#).

6. **Deep Neural Network (DNN):** Universal function approximator. DNNs relate input and output through non-linear mappings.

5.11.4. HYPERPARAMETER SETTINGS

We sample 100 hyperparameters, train each model on test set and evaluate on the validation set to find the optimum parameters for learning a train-test split. We then test the models on the remaining test fold. We do this 5 times. We use NVIDIA RTX 2080 graphics card for training neural models.

The hyperparameter search space of the models are as follows:

LIN

- Regressor

```
param_grid = {  
  "C": [5e-2, 1e-1, 5e-1, 1],  
  "max_iter": [5000]  
}
```

- Classifier

```
param_grid = {  
  "C": [5e-2, 1e-1, 5e-1, 1],  
  "max_iter": [5000]  
}
```

EBM

- Regressor

```
param_grid = {  
  "outer_bags": [8, 25, 75, 100],  
  "inner_bags": [0, 1, 2, 5, 10]  
}
```

- Classifier

```
param_grid = {  
  "outer_bags": [8, 25, 75, 100],  
  "inner_bags": [0, 1, 2, 5, 10]  
}
```

RF

- Regressor

```
param_grid = {  
  "ccp_alpha": [0.0, 1e-1, 1e-2],  
  "max_depth": [None, 4, 8, 16, 40, 100],  
  "min_samples_leaf": [1, 3, 5, 10],  
  "min_samples_split": [2, 4, 6, 12],  
  "n_estimators": [100, 200, 600, 800]  
}
```

- Classifier

```
param_grid = {  
  "ccp_alpha": [0.0, 1e-1, 1e-2],  
  "max_depth": [None, 4, 8, 16, 40, 100],  
  "min_samples_leaf": [1, 3, 5, 10],  
  "min_samples_split": [2, 4, 6, 12],  
  "n_estimators": [100, 200, 600, 800]  
}
```

LGBM

- Regressor

```
param_grid = {
  "num_leaves": [31, 50, 70, 100],
  "max_depth": [-1, 5, 7, 10],
  "learning_rate": [0.001, 0.01, 0.05, 0.1],
  "n_estimators": [100, 200, 500],
  "subsample_for_bin": [200000, 500000],
  "min_split_gain": [0.0, 0.1, 0.5],
  "min_child_weight": [1e-3, 1e-2, 1e-1, 1],
  "min_child_samples": [20, 30],
  "subsample": [0.8, 0.9, 1.0],
  "colsample_bytree": [0.7, 0.8, 0.9, 1.0],
  "reg_alpha": [0, 1, 2],
  "reg_lambda": [0, 1, 2],
  "boosting_type": ['gbdt', 'dart'],
}
```

- Classifier

```
param_grid = {
  "num_leaves": [31, 50, 70, 100],
  "max_depth": [-1, 5, 7, 10],
  "learning_rate": [0.001, 0.01, 0.05, 0.1],
  "n_estimators": [100, 200, 500],
  "subsample_for_bin": [200000, 500000],
  "min_split_gain": [0.0, 0.1, 0.5],
  "min_child_weight": [1e-3, 1e-2, 1e-1, 1],
  "min_child_samples": [20, 30],
  "subsample": [0.8, 0.9, 1.0],
  "colsample_bytree": [0.7, 0.8, 0.9, 1.0],
  "reg_alpha": [0, 1, 2],
  "reg_lambda": [0, 1, 2],
  "boosting_type": ['gbdt', 'dart'],
}
```

XGB

- Regressor param_grid = {

```
"learning_rate" : [0.05, 0.10, 0.15, 0.30],
"max_depth" : [3, 5, 8, 15],
"min_child_weight" : [1, 3, 7],
"gamma" : [0.0, 0.1, 0.3],
"colsample_bytree" : [0.3, 0.4, 0.5],
'ccp_alpha': [0.0,1e-3,1e-2],
"min_impurity_decrease": [0, 1e-1]
}
```

- Classifier

```
param_grid = {
  "learning_rate" : [0.05, 0.10, 0.15, 0.30],
  "max_depth" : [3, 5, 8, 15],
  "min_child_weight" : [1, 3, 7],
  "gamma" : [0.0, 0.1, 0.3],
  "colsample_bytree" : [0.3, 0.4, 0.5],
  'ccp_alpha': [0.0,1e-3,1e-2],
  "min_impurity_decrease": [0, 1e-1]
}
```

DNN

- Regressor

```
param_grid = { "batch_size": [1024, 512],
  "lr":[5e-4, 1e-3, 2e-3],
  "act": ['relu', 'snake', 'elu'],
  "norm":[None, 'layer', 'batch'],
  "n_layers":[2, 3, 4, 5],
  "d_hid":[25, 50, 75, 100, 200],
  "weight_decay": [0, 1e-10, 1e-8, 1e-6],
  "dropout": [0, 0.2, 0.4, 0.5],
}
```

- Classifier

```
param_grid = { "batch_size": [1024, 512],
  "lr":[5e-4, 1e-3, 2e-3],
  "act": ['relu', 'snake', 'elu'],
  "norm":[None, 'layer', 'batch'],
  "n_layers":[2, 3, 4, 5],
  "d_hid":[25, 50, 75, 100, 200],
  "weight_decay": [0, 1e-10, 1e-8, 1e-6],
  "dropout": [0, 0.2, 0.4, 0.5],
}
```

VSN

- Regressor


```
param_grid = { "batch_size": [1024],
                "lr":[1e-3],
                "act": ['relu', 'snake', 'elu'],
                "norm":[None, 'layer'],
                "n_layers":[4],
                "d_hid":[150],
                "weight_decay": [0],
                "dropout": [0],
                "p_missing":[1/2, 2/3, 'shapley'],
                "train_phi0":[True, False]
              }
```
- Classifier


```
param_grid = { "batch_size": [1024],
                "lr":[1e-3],
                "act": ['relu', 'snake', 'elu'],
                "norm":[None, 'layer'],
                "n_layers":[4],
                "d_hid":[150],
                "weight_decay": [0],
                "dropout": [0],
                "p_missing":[1/2, 2/3, 'shapley'],
                "train_phi0":[True, False]
              }
```

For our VSN architecture, we employ a 4-layer masked embedding network, followed by a 4-layer feedforward neural network, each with 150-dimensional layers. The embedding dimensions are fixed at 50. We conduct experiments involving the tuning of activation functions and investigating missing data handling. Specifically, we set the parameter p to values of 1/2, 2/3, or align it with the Shapley permutation distribution denoted as $p(s|C)$. Additionally, we make a choice between training ϕ_0 or keeping it fixed at the average dataset y . The rationale for the latter choice is that the learned ϕ_0 is expected to naturally converge toward this value, or close to it. Therefore, by initializing it with this average dataset response, we facilitate this convergence process.

5.12. Results: Predictive Performance Averages and Standard Errors

In this section, we present the average predictive results with their corresponding standard error values for both real world and simulated data.

Data	Self-explaining			Black-box			
	VSN	LIN	EBM	RF	LGBM	XGB	DNN
PKSN	0.031 ± 0.003	0.867 ± 0.009	0.195 ± 0.002	0.040 ± 0.006	0.072 ± 0.009	0.063 ± 0.002	0.111 ± 0.005
MED	0.447 ± 0.018	0.608 ± 0.015	0.447 ± 0.021	0.448 ± 0.018	0.447 ± 0.020	0.454 ± 0.016	0.467 ± 0.005
BIKE	0.010 ± 0.001	0.518 ± 0.004	0.038 ± 0.001	0.008 ± 0.001	0.017 ± 0.002	0.013 ± 0.001	0.019 ± 0.001
PUMA	0.285 ± 0.003	1.005 ± 0.005	0.326 ± 0.004	0.303 ± 0.005	0.334 ± 0.015	0.345 ± 0.009	0.225 ± 0.003
GAS	0.273 ± 0.043	60.93 ± 60.060	0.153 ± 0.016	0.151 ± 0.015	0.152 ± 0.012	0.150 ± 0.021	0.256 ± 0.019
WINE	0.474 ± 0.021	0.561 ± 0.561	0.508 ± 0.018	0.478 ± 0.019	0.439 ± 0.019	0.433 ± 0.018	0.444 ± 0.015
ELEV	0.350 ± 0.003	0.593 ± 0.100	0.385 ± 0.002	0.457 ± 0.004	0.373 ± 0.002	0.373 ± 0.001	0.341 ± 0.003
FICO	0.774 ± 0.004	0.766 ± 0.004	0.771 ± 0.004	0.770 ± 0.003	0.773 ± 0.005	0.773 ± 0.004	0.771 ± 0.007
SPAM	0.977 ± 0.003	0.946 ± 0.006	0.977 ± 0.003	0.983 ± 0.002	0.982 ± 0.002	0.981 ± 0.003	0.967 ± 0.005
ICU	0.869 ± 0.004	0.851 ± 0.004	0.872 ± 0.004	0.869 ± 0.004	0.874 ± 0.003	0.874 ± 0.003	0.860 ± 0.004
CENS	0.795 ± 0.003	0.768 ± 0.003	0.825 ± 0.003	0.800 ± 0.002	0.830 ± 0.003	0.831 ± 0.004	0.788 ± 0.003

Table 3. VSN and baseline comparison across real-world datasets.

Net	β	synth1	synth2	synth3	synth4	synth5
Masked	0.001	0.647 \pm 0.020	0.003 \pm 0.000	0.104 \pm 0.004	0.675 \pm 0.016	0.430 \pm 0.008
	0.01	0.637 \pm 0.017	0.004 \pm 0.001	0.097 \pm 0.004	0.674 \pm 0.020	0.421 \pm 0.007
	0.1	0.637 \pm 0.018	0.003 \pm 0.000	0.114 \pm 0.014	0.668 \pm 0.017	0.414 \pm 0.005
	1	0.595 \pm 0.012	0.006 \pm 0.001	0.265 \pm 0.019	0.665 \pm 0.020	0.389 \pm 0.010
Vanilla	0.001	0.694 \pm 0.012	0.005 \pm 0.000	0.590 \pm 0.037	0.674 \pm 0.013	0.442 \pm 0.003
	0.01	0.685 \pm 0.026	0.004 \pm 0.000	0.379 \pm 0.113	0.680 \pm 0.017	0.437 \pm 0.007
	0.1	0.668 \pm 0.018	0.071 \pm 0.062	0.444 \pm 0.089	0.687 \pm 0.017	0.471 \pm 0.043
	1	1.258 \pm 0.572	0.209 \pm 0.070	0.752 \pm 0.108	0.680 \pm 0.016	1.088 \pm 0.423

Table 4. Comparison to vanilla network without missingness indicators (ξ) in simulated datasets.

Net	β	synth1	synth2	synth3	synth4	synth5
Masked	0.001	0.647 \pm 0.020	0.003 \pm 0.000	0.104 \pm 0.004	0.675 \pm 0.016	0.430 \pm 0.008
	0.01	0.637 \pm 0.017	0.004 \pm 0.001	0.097 \pm 0.004	0.674 \pm 0.020	0.421 \pm 0.007
	0.1	0.637 \pm 0.018	0.003 \pm 0.000	0.114 \pm 0.014	0.668 \pm 0.017	0.414 \pm 0.005
	1	0.595 \pm 0.012	0.006 \pm 0.001	0.265 \pm 0.019	0.665 \pm 0.020	0.389 \pm 0.010
Vanilla	0.001	0.718 \pm 0.023	0.004 \pm 0.000	0.462 \pm 0.090	0.679 \pm 0.017	0.448 \pm 0.005
	0.01	0.666 \pm 0.016	0.004 \pm 0.000	0.358 \pm 0.108	0.678 \pm 0.017	0.444 \pm 0.007
	0.1	0.650 \pm 0.009	0.007 \pm 0.001	0.231 \pm 0.073	0.670 \pm 0.016	0.439 \pm 0.009
	1	0.640 \pm 0.019	0.018 \pm 0.003	0.782 \pm 0.296	0.670 \pm 0.017	0.523 \pm 0.086

Table 5. Comparison to vanilla network with missingness indicators (ξ) in simulated datasets.

5.13. A DGP with Stochastic Shapley Values

We consider synthetic1 dataset with below generative process.

For $i = 1, 2, \dots, N$:

- (i) Draw $x_1^{(i)}, x_2^{(i)}, x_3^{(i)} \sim U(-4, 4)$,
- (ii) Draw $\varphi_1^{(i)} \sim \mathcal{N}\left(2 + \exp\{-x_1^{(i)2}\}, 0.6 \cos(0.03x_1^{(i)800})\right)$, $\varphi_2^{(i)} \sim \mathcal{N}\left(1 + \sin(-x_2^{(i)2}), 0.2|x_2^{(i)}|\right)$, and $\varphi_3^{(i)} = 3 \cos(3x_3^{(i)}) + 4 \sin(5x_3^{(i)})$,
- (iii) Calculate $y^{(i)} = \varphi_1^{(i)} + \varphi_2^{(i)} + \varphi_3^{(i)}$.

The observed data are $\{\mathbf{x}^{(i)}, y^{(i)}\}_{i=1}^N$ pairs.

Given the functional forms of the true DGP and the additive nature of y , ESVs can be easily computed via $\phi_j = \mathbb{E}_{p(y_j|x_j)}\{y_j - \mathbb{E}_{p(x_j)}\{y_j\}\}$. For example, the ESV of x_1 is $\exp\{-x_1^2\} - \int U(-4, 4) \exp\{-x_1^2\} dx_1 = \exp\{-x_1^2\} - \frac{\sqrt{\pi}}{8} \operatorname{erf}(4)$, x_2 is $1 + \sin(-x_2^2) - \int U(-4, 4) (1 + \sin(-x_2^2)) dx_2 = \sin(-x_2^2) + \frac{\sqrt{2\pi}}{8} S(4\sqrt{\frac{2}{\pi}})$, where $S(\cdot)$ is the Fresnel integral, and the ESV of x_3 is $3 \cos(3x_3) + 4 \sin(5x_3) - \int U(-4, 4) (3 \cos(3x_3) + 4 \sin(5x_3)) dx_3 = 3 \cos(3x_3) + 4 \sin(5x_3) - \frac{1}{4} \sin(12)$.

As demonstrated by the above equations, ESVs do not give the *exact* contribution of an individual feature x_j , on the random outcome y , but informs on average how x_j contributes to y , where the average is calculated via $p(y_j|x_j)$ (which corresponds to the location parameter of the normal distributions described above) and shifted using the marginal $p(x_j) = U(-4, 4)$. However, the variance of y_j can be high, as exemplified in our generative process and Fig. 4, and therefore, each individual contribution of examples might vary. In this paper, we show that VSN captures this variability in contributions.

5.14. Explainability on Real-world Dataset: A Case Study on Intensive Care Unit Patients

Global explanations. Fig. 6 shows estimated Shapley values for 21 clinical features used to predict patient mortality. Medically trained collaborators assisted in interpreting this figure.

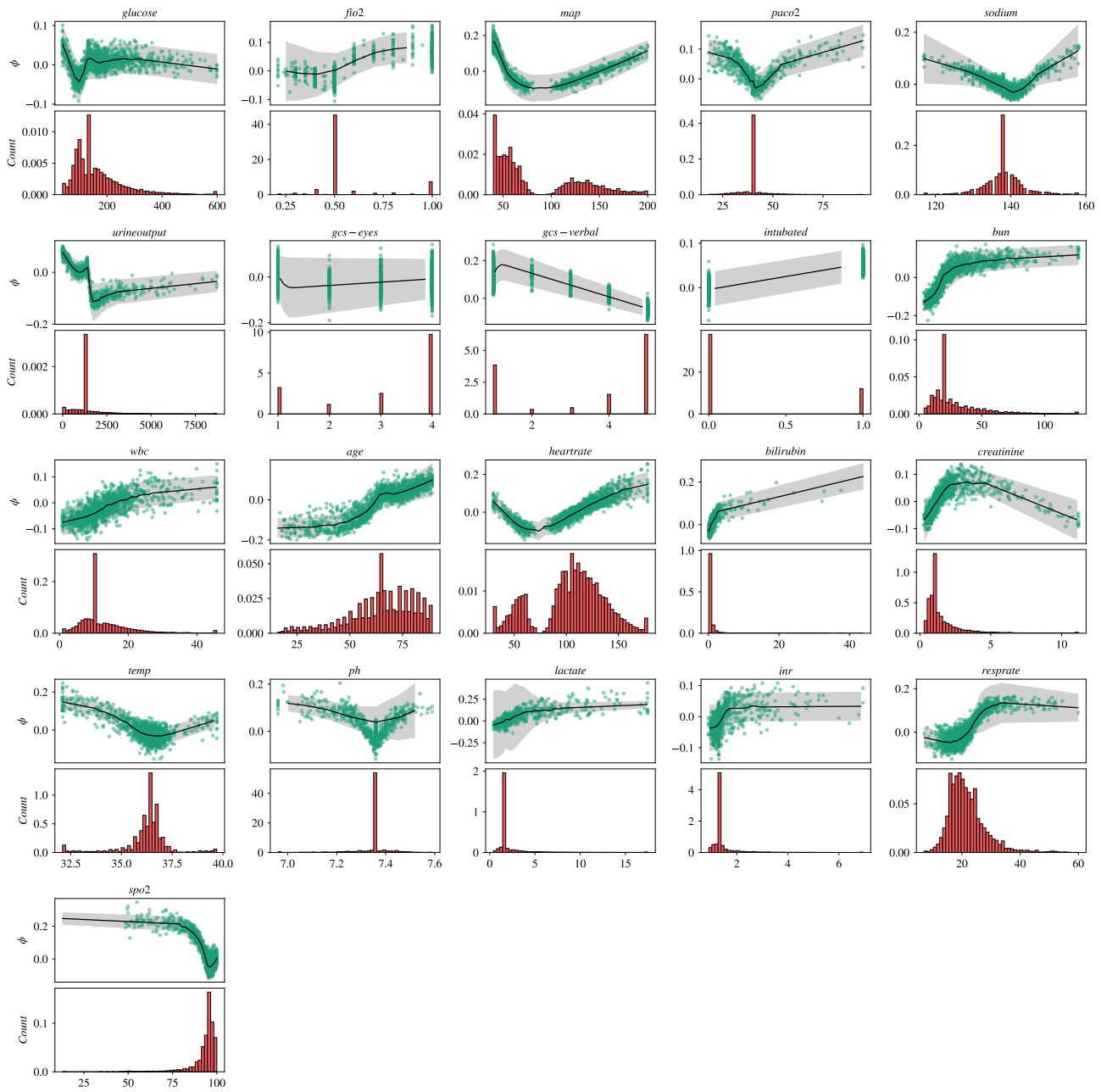


Figure 6. Location (Shapley values, μ_θ) and scale parameters (1 standard deviation around the mean, σ_ψ) of SSV prior. The higher values imply higher chances of mortality. We fit a smooth curve (black) around the Shapley values to demonstrate the trend and shade the areas around it with respect to the standard deviation given by SSV prior. Larger shaded regions imply more uncertain feature contributions, while less shaded regions imply certainty regarding feature contribution. As an example, mean arterial blood pressure (map) and bilirubin are strong indicators of mortality (with less uncertainty), the contribution of fractional concentration of oxygen (fio2) and glucose to mortality exhibits high variance.

Several features such as WBC, lactate, INR, and BUN display monotonically increasing Shapley values. This is sensible, since higher values for these variables confer worse patient state (infection, inflammation, reduced coagulability, renal

insufficiency, respectively). Similarly, Shapley values for Glasgow coma scale (GCS) variables decrease monotonically. This is consistent as lower GCS scores imply the patient is less conscious.

Other features display non-monotonic Shapley values. These variables have a relatively narrow normal range outside of which patient state may decline. For example, normal temperature is 36.5° - 37.5° C and corresponds to a Shapley value nadir. Similar Shapley value nadirs are observed at the normal ranges for heart rate (60-100 BPM), respiratory rate (15-20 BPM), pH (7.32-7.42), urine output (.8-2L), and sodium (135-145 mEq/L).

Local explanations. Fig. 7 presents the mortality prediction for four unique patients, highlighting both the prior predictive mean (labeled as Pred') and the associated uncertainty (labeled as Err') along with feature specific SSV uncertainties.

The uncertainty embedded in these predictions is vital for clinicians to understand the potential severity of a patient's condition. For example, patients that are seemingly in good conditions can unexpectedly turn critical. This variance is captured in VSN through the predictive uncertainty. Such insights are invaluable, particularly in high-stakes environments like the ICU, where they can guide clinical decisions by acknowledging the inherent variability in patient outcomes.

The uncertainty in SSVs informs clinicians on how critical each feature is for patient outcome variability. For example, predictions of False positive patients exhibit high variability due to lactate, raising important questions: Why does this biomarker exhibit high outcome variability for this patient? How do we reduce the variability caused by this biomarker?

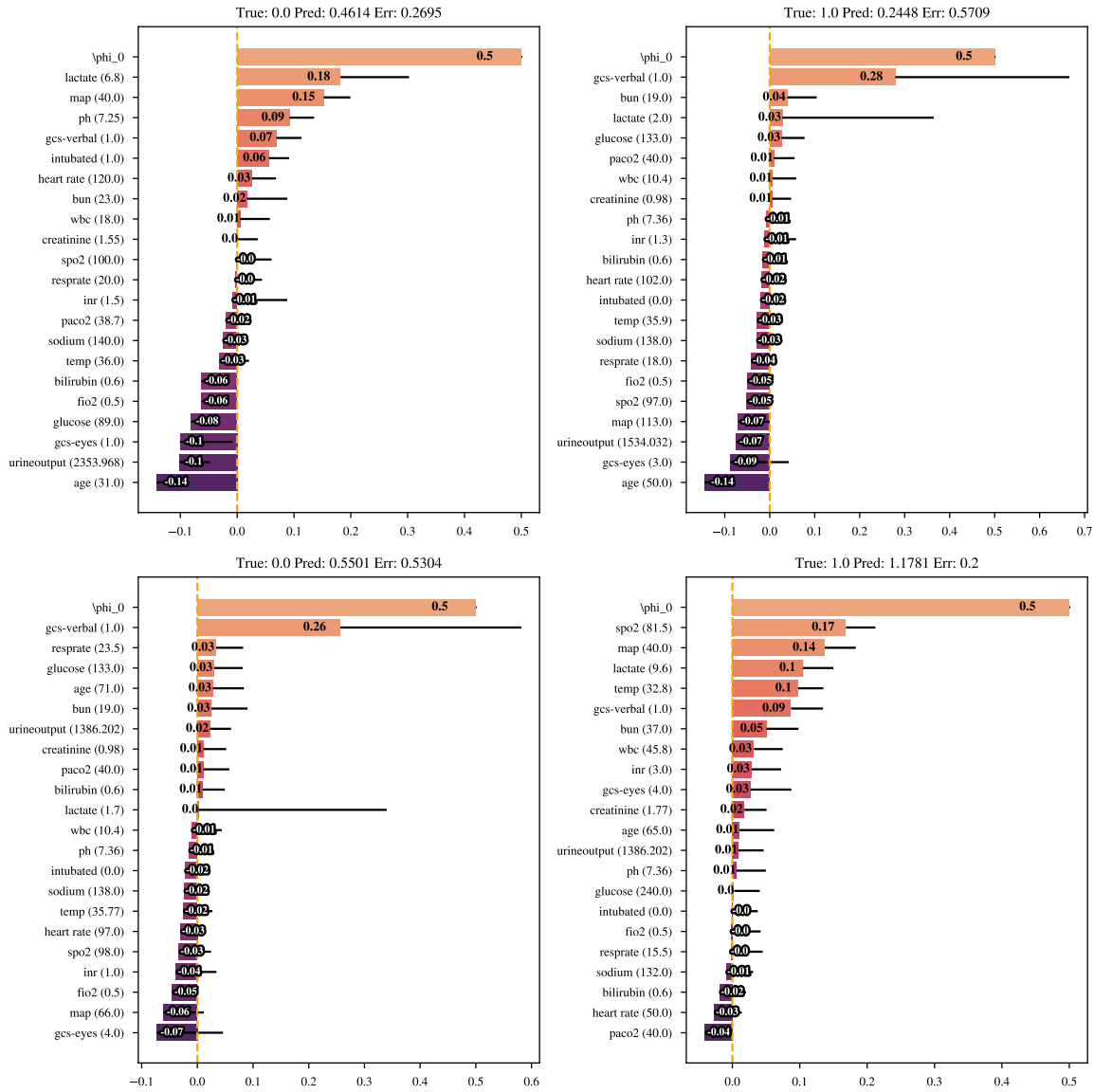


Figure 7. Assessment of VSN’s interpretability across four distinct ICU patients for mortality prediction on a confusion table. ‘True’ represents actual outcomes, ‘Pred’ stands for model predictive mean (sum of ESVs and ϕ_0), and ‘Err’ reflects the overall uncertainty in predictions. ESVs for specific features are denoted by colored bars, whereas the uncertainty in these variables is marked by black lines. Elevated uncertainty in explanatory variables should prompt practitioners to reconsider both the significance of these features and the reliability of the predictions.

5.14.1. RELEVANCE AND APPLICATIONS

Importance of the global view. The plots mentioned previously play a crucial role in model diagnostics. For instance, [Caruana et al. \(2015\)](#) discovered that in predicting the risk of pneumonia, models tend to allocate lower risk scores to patients with asthma using such global view plots. This phenomenon arises from the intensive treatments typically administered to patients with these coexisting conditions. Uncritically accepting these low-risk scores from models for patients could result in inappropriate non-hospitalization of patients who are actually in poor health.

In our case, we observe that the model cannot capture optimum creatinine values: The model assigns lower mortality to high creatinine values, which is counterintuitive. This might be due to a confounder affecting the contributions of creatinine that need further investigation. VSN informs practitioners regarding such pathologies in data.

Reasoning about trustworthy features. While we observe that features like map, sodium, bilirubin, gcs-verbal demonstrate smaller variance values, glucose, fio2, inr, gcs-eye demonstrates higher variance values.

For example, glucose is not a reliable indicator of ICU mortality, as high glucose levels can be associated with several non-fatal pathologies such as dehydration, over-treating hypoglycemia, and diabetes. While these conditions are not directly lethal, they may lead to more serious complications like heart-related problems. Elevated glucose levels should thus be interpreted within a broader clinical context, taking into account a patient's overall health and medical history. This comprehensive approach is crucial because, although not directly fatal, these conditions can contribute to long-term health issues that increase mortality risk, making glucose a significant but not solitary indicator of health status.

As another example, the international normalized ratio (INR), a key measure of blood clotting used particularly for patients on anticoagulants like warfarin, is influenced by a range of factors including diet, certain medications, alcohol consumption, and liver function. These factors contribute to the variability of INR values, making them less reliable as sole indicators of ICU mortality. Diet, especially foods rich in vitamin K, can affect INR levels, as can interactions with various drugs. Alcohol use has a complex relationship with INR; chronic use may increase it, while acute use can have the opposite effect. Additionally, liver health is crucial, as it plays a vital role in producing clotting factors. This variability, along with the influence of external factors, underscores the challenge of using INR values alone to accurately infer ICU mortality, reflecting the need for a comprehensive assessment of a patient's overall health and medical history in critical care settings.

Knowing the variability of explanations is important to summarize/filter the information (i.e., what to present to the practitioners) where summarizing accurate information in a short time periods is crucial in time-sensitive settings such as treating ICU patients.